Atmospheric Research 324 (2025) 108203

Contents lists available at ScienceDirect

Atmospheric Research

journal homepage: www.elsevier.com/locate/atmosres

Transition of dominant cloud microphysical processes for increasing lightning preceding downbursts in multi-cell convective clouds

Makoto Kondo [a,1,*], Yousuke Sato [b,c,2]

[a] Graduate School of Science, Hokkaido University, Hokkaido, Japan,
[b] Faculty of Science, Hokkaido University, Hokkaido, Japan
[c] RIKEN Center for Computational Science, Hyogo, Japan

ARTICLE INFO

Keywords:
Cloud microphysics
Numerical simulation
Bulk lightning model
Downburst
Graupel

ABSTRACT

Based on the results of numerical simulations, a possible mechanism for the occurrence of a rapid increase in lightning frequency preceding a downburst was investigated according to cloud microphysical processes in mixed-phase areas. To elucidate the mechanism, idealized experiments were conducted targeting multi-cell convective clouds using a meteorological model coupled with a bulk lightning model, which explicitly calculates riming, charge separation via riming electrification, and lightning discharge. The model well reproduced a rapid increase in the lightning flash rate in multi-cell convective clouds approximately 15 min before a downburst. In a convective cell during increasing flash rate, solid hydrometeors were supplied to the convective area and riming electrification occurred actively. In contrast, in a convective cell that caused a downburst, riming occurred actively because of the supply of a large amount of supercooled water from the lower layers. A convective cell suitable for riming electrification or graupel growth by riming occurred when the convection was or was not tilted, respectively. The transition from tilted convection suitable for riming electrification to upright convection suitable for active riming growth is critical for the occurrence of the rapid increase of lightning preceding downbursts.

1. Introduction

In deep convective mixed-phase clouds, solid particles can grow by collisions involving supercooled water, known as riming (riming growth), which produces dense solid particles such as graupel and hail (Pruppacher and Klett, 1997; Brdar and Seifert, 2018; List, 1961, 2014). These high-density solid particles can intensify downdrafts near the surface via drag force and cooling by evaporation, sublimation, and melting. According to previous reports, such downdrafts can sometimes result in appreciable downbursts with wind velocities exceeding 12 ft. s^{-1} at 300 ft.; 3.66 m s^{-1} at 91.4 m above the surface (Fujita and Byers, 1977; Fujita, 1985; Wakimoto, 1985; Wilson et al., 1984; Hjelmfelt, 1988; Fujita, 1992; Wilson and Wakimoto, 2001).

Another distinctive cloud microphysical process related to collisions in deep convective mixed-phase clouds is charge separation through riming electrification, which was reported originally in laboratory experiments (e.g., Takahashi, 1978; Saunders et al., 1991). Riming electrification occurs through the collision and rebound of rimed ice crystals or graupel with ice or snow particles (Takahashi, 1978; Saunders et al., 1991), and riming electrification is one of the main processes for charge generation in thunderstorms, and the charged particles generated via charge separation can lead to lightning.

The above background indicates that riming growth and riming electrification induce the occurrence of severe disastrous weather events such as heavy rainfall, hailstorms, downbursts, and lightning. To identify precursors to severe weather associated with deep convective clouds, the relationship between lightning and severe weather has been examined recently. Lightning frequency increases rapidly preceding severe weather related to riming growth, such as heavy rainfall, hail, and downbursts (e.g., Goodman et al., 1988; Williams et al., 1999; Schultz et al., 2009, 2011; Farnell and Rigo, 2020; Erdmann and Poelman, 2023). Sometimes called a lightning jump (LJ) (Goodman et al., 1988; Williams et al., 1999; Schultz et al., 2009, 2011, 2017), this rapid increase in lightning frequency is used to predict severe weather events

* Corresponding author.
E-mail addresses: konchasu56@eei.eng.osaka-u.ac.jp (M. Kondo), yousuke.sato@civil.eng.osaka-u.ac.jp (Y. Sato).
[1] Present affiliation: Division of Electrical Electronic and Infocommunications, Graduate School of Engineering, The University of Osaka, Suita, Osaka, Japan.
[2] Present affiliation: Division of Global Architecture, Graduate School of Engineering, The University of Osaka, Suita, Osaka, Japan.

https://doi.org/10.1016/j.atmosres.2025.108203
Received 6 October 2024; Received in revised form 24 April 2025; Accepted 6 May 2025
Available online 11 May 2025

(e.g., Schultz et al., 2009, 2011; Farnell and Rigo, 2020; Gatlin and Goodman, 2010; Erdmann and Poelman, 2023). Combined analyses of radar and lightning observations have contributed considerably to understanding the relationship between severe weather and LJs. Schultz et al. (2015, 2017) investigated the kinematic and cloud microphysical characteristics of LJs by using the three-dimensional bulk characteristics of particle types and fall velocities retrieved from the Advanced Radar for Meteorological and Operational Research (Knupp et al., 2014) and KHTX radar data, as well as total lightning data from the North Alabama Lightning Mapping Array (Koshak et al., 2004; Goodman et al., 2005). Schultz et al. (2015) examined the relationship between LJs and the trends in mixed-phase graupel mass, maximum updraft velocity, and updraft volume, and they reported that LJs occurred when the updraft volume whose velocity reached 10 m s^{-1} and the mixed-phase graupel mass increased. The relationship between updrafts and lightning frequency is well established, as updrafts exceeding 10 m s^{-1} contribute to an increase in the number concentration of ice particles aloft (Dye et al., 1986; Schultz et al., 2015) and result in both active riming and riming electrification within the updraft areas of deep convective clouds.

However, there is scope for further investigation into the relationship among lightning frequency, graupel mass, and updraft intensity. Deierling et al. (2008) reported a tenfold difference in total lightning frequency for clouds with similar graupel masses. Several other studies have reported that lightning originating from riming electrification tends to occur in areas where hail produced by the riming growth is absent. Known as lightning holes (Krehbiel et al., 2000; MacGorman et al., 2005; Emersic et al., 2011; Ni et al., 2023), such areas have been observed in supercell cases with mesocyclones (Krehbiel et al., 2000; MacGorman et al., 2005) and in other thunderstorm cases (Emersic et al., 2011). The clouds that produce lightning holes suggest that the lightning holes are governed by not only the kinematic structure of the clouds but also their microphysical processes. Emersic et al. (2011) indicated that the occurrence of lightning holes could be due to the environment conducive to riming growth of hail being unsuitable for charge separation, based on observations from the National Weather Radar Testbed Phased-Array Radar.

These reports from previous studies imply that the whole complicated relationship among hydrometeors, including supercooled water, ice, snow, graupel, and hail, as well as riming growth, riming electrification, and other cloud microphysical processes should be considered in order to elucidate the relationship between lightning and severe weather.

Observational studies that used the characteristics of graupel and lightning as proxies for the cloud microphysical properties of mixed-phase areas have provided valuable insights into the mechanisms behind LJs. However, there are challenges associated with using radar observations to analyze the cloud microphysics of mixed-phase areas. While radar can capture the entire cloud and analyze particle characteristics within it using hydrometeor classification methods (Park et al., 2009; Dolan et al., 2013), it struggles to accurately represent the coexistence of ice and liquid water particles, which is crucial in mixed-phase areas. Consequently, clarifying the physical processes within mixed-phase clouds—where riming growth and riming electrification either coexist or are in conflict—is essential to clarify their mechanisms and advance our understanding of cloud microphysical processes and their effects on LJs.

Numerical studies using meteorological models have advantages for analyzing mixed-phase clouds because they provide dense three-dimensional data that can represent the coexistence of solid and liquid particles in mixed-phase areas. Additionally, by utilizing meteorological models coupled with bulk lightning models (Sato et al., 2019; Fierro et al., 2013; Barthe et al., 2012), we can investigate mixed-phase areas conducive to lightning and downbursts. In a bulk lightning model, the charge separation processes are calculated explicitly from the collision and rebound processes between graupel and ice/snow within cloud microphysical schemes based on riming electrification (Takahashi, 1978; Saunders et al., 1991), and the electric field generated by the calculated charge distribution can be used to represent lightning as the neutralization of these charge imbalances. Meteorological models coupled with bulk lightning models enable the investigation of complex charge distributions within convective clouds based on dynamical and cloud microphysical processes including riming growth and riming electrification (Chen et al., 2020; Sato et al., 2019, 2022). Recent studies have utilized meteorological models coupled with bulk lightning models to examine the correlation between severe weather and lightning activity. Luque et al. (2023) investigated the correlation between severe weather in convective clouds and lightning activity observed during field campaigns using Weather Research and Forecasting with the ELECtrification (WRF-ELEC; Fierro et al., 2013); however, that study was focused on identifying good proxies for LJs, such as hail and strong wind, rather than analyzing the physical mechanisms between hail and lightning activity such as an LJ.

Thus, previous studies have been limited to separate the suitable condition for riming process and that for riming electrification, which is critical to understand the LJ. Numerical experiments using a meteorological model coupled with a bulk lightning model enable us to examine the riming growth and riming electrification separately, and the simulations could bridge the gap in understanding the mechanism of LJs and that by previous studies.

The aim herein is to suggest a possible mechanism for a LJ, characterized by the rapid increase of lightning flash rate associated with riming electrification, which precedes the downburst associated with riming growth in mixed-phase clouds. To achieve this, we use a meteorological model coupled with a bulk lightning model.

2. Data and methods

2.1. Target case

To achieve the aims of this study, idealized experiments were conducted focusing on the downburst that occurred in Misato Town in Saitama Prefecture in Japan on 8 September 1994, a day that saw the occurrence of multi-cell convective clouds involving multiple downbursts and lightning (Takayama et al., 1997). As the first step, we selected multi-cell convective clouds because with them the correlation between LJs and downbursts is stronger than with isolated convective clouds (Rigo and Farnell, 2022).

2.2. Model description and experimental setup

Idealized experiments were conducted using the SCALE (Scalable Computing for Advanced Library and Environment) (Nishizawa et al., 2015; Sato et al., 2015) meteorological model coupled with a bulk lightning model (Sato et al., 2019). The bulk lightning model calculates the charges of cloud hydrometeors as prognosis variables: the riming electrification due to graupel-snow and graupel-ice collisions and rebounding is calculated using a look-up table based on Takahashi (1978). And the flash origin density (FOD) corresponding to flash frequency is calculated using the neutralized scheme by Fierro et al. (2013); see Sato et al. (2019) for the details of the bulk lightning model. The other physical schemes are summarized in Appendix B. The cloud microphysical scheme used in this study (Seiki and Nakajima, 2014) represents cloud hydrometeors by the five categories of cloud, rain, cloud ice, snow, and graupel. The hail category is not treated by the model, but the drag force due to heavy solid hydrometeors, which is critical to downbursts, can be reproduced by heavy graupel. The calculation domain covered 180 km × 120 km in the x and y directions, respectively, with 0.1-km horizontal grid spacing with doubly periodic boundary conditions, and 100 vertical layers with gradually increasing layer thickness from 0.01 km to 1.578 km (the model top is 20.4 km) were used. The calculation time was 90 min, and the output interval was 20 s. Rayleigh damping was applied above 15 km, and a free-slip surface

boundary was adopted.

The horizontally uniform initial vertical profiles of potential temperature, water vapor mixing ratio, and horizontal wind were obtained from sounding data measured at Maebashi and Tateno, with the data from Tateno used to supplement the lack of wind data at Maebashi on the day described in Section 2.1 (Guo et al., 1999) (Appendix A), and the surface pressure was set as 992.8 hPa at the initial time. We conducted two experiments to investigate the relationship between lightning activity and downburst. The control experiment was conducted using the initial vertical profiles of the original sounding data (Guo et al., 1999). For the sensitivity experiment, called the strong shear experiment, only the horizontal wind shear in the x direction was increased by 20 % from its vertical profile used in the control experiment (dash-dotted line in Fig. A1b in Appendix A).

To trigger convection, we inserted a potential-temperature perturbation θ' [Eq. (C1), following Miyamoto (2021)] at $(x, y, z) = (160, 20, 0.5)$ km in the calculation domain, where the origin is set at the southwest corner of the domain at the initial time.

2.3. Definitions of lightning increase preceding downburst corresponding to lightning jump and heavy graupel

Various algorithms have been proposed for defining a LJ, such as the 2σ LJ algorithm for the increase in lightning frequency every 2 min (Schultz et al., 2009, 2011; Farnell et al., 2017), and the Relative Increase Level algorithm for the Geostationary Lightning Mapper, which calculates simple lightning frequency increments (Erdmann and Poelman, 2023). However, these LJ algorithms require thresholds for the target severe weather, and these thresholds depend on observational instruments. Also, it is not easy to apply these algorithms to the output of the model, so we simply defined a "preceding lightning increase" corresponding to a LJ as an increase in lightning activity continuing for at least 5 min preceding the occurrence of a downburst. This definition is not the same as those used in previous studies, which aimed to evaluate lead times and warning accuracy for severe phenomena. However, the definition used in the present study does not focus on predictive accuracy but rather emphasizes the relationship between the increase in lightning activity and subsequent downbursts. In addition, Schultz et al. (2011) reported that total lightning, which is the sum of cloud-to-ground and intra-cloud discharges, is a superior LJ indicator, so we used FOD as the lightning frequency, which corresponds to total lightning in the model.

For analyzing the downburst, we focused on the heavy graupel simulated by the model, which corresponds to hail in nature. Graupel weight itself is not affect the charge separation amount per one collision, however, the calculation of heavy graupel was conducted solely for the analysis of graupel contributing to downburst. Heavy graupel was defined as that with a mean particle mass m_g exceeding 50 mg; m_g was calculated as $m_g = \rho Q_g / N_g$, where $\rho, Q_g,$ and N_g are respectively the graupel density, mass mixing ratio, and number concentration predicted by the model.

2.4. Analysis of convection tilting, horizontal flux, and vertical flux

To investigate the influence of wind circulation, we examined the impacts of liquid water supply from lower layers on the riming growth and the supply of solid hydrometeor particles from the surrounding area on the riming electrification according to the vertical mass flux of liquid water (WQ_{liq}) and the horizontal flux of the snow number concentration (UN_S), respectively. The quantities UN_S and WQ_{liq} are defined as

$$UN_S = U_{\mathrm{horiz}} N_S, \tag{1}$$

where N_S is the number concentration of snow and U_{horiz} is the absolute horizontal wind velocity, and

$$WQ_{\mathrm{liq}} = W\rho(q_R + q_C), \tag{2}$$

where q_R and q_C are the mixing ratios of rain and cloud water, respectively, and W is the vertical wind velocity. UN_S represents the horizontal supply of snow particles and could contribute to the enhancement of graupel-snow collisions and rebounding, which are crucial for the charge separation process during riming. WQ_{liq} indicates the supply of liquid water from the lower layers and could promote graupel growth through riming.

The convection tilting angle φ_{tilt} is calculated as

$$\varphi_{\mathrm{tilt}} = \arctan\left(\frac{W}{U_{horiz}}\right) \left(-\frac{\pi}{2} \le \varphi_{tilt} \le \frac{\pi}{2}\right). \tag{3}$$

In this study, convection with $\varphi_{\mathrm{tilt}} > \frac{5}{18}\pi$ is defined as upright convection, that with $\varphi_{tilt} < \frac{\pi}{6}$ is defined as tilted convection, and that with $\frac{\pi}{6} < \varphi_{\mathrm{tilt}} \le \frac{5}{18}\pi$ is defined as moderate convection.

Also, to interpret the results from the present numerical experiments on multi-cell convective clouds, we use the parameter $C/\Delta U$ (Rotunno et al., 1988; Weisman and Rotunno, 2004; Takemi, 2006; Lebo and Morrison, 2014), where C and ΔU represent cold pool intensity and vertical wind shear, respectively. This parameter was introduced by previous studies (Rotunno et al., 1988; Weisman and Rotunno, 2004) as part of the Rotunno–Klemp–Weisman (RKW) theory in order to discuss optimal convection structures, and it was reported that $C/\Delta U \sim 1$ and $C/\Delta U \gg 1$ are optimal conditions for upright convection and tilted convection, respectively, at the leading edge of the cold pool. Therefore, we calculated $C/\Delta U$ for our results to examine suitable environments for tilted or upright convection, with C, B, and ΔU defined in Takemi (2006) in Appendix C:

3. Results

3.1. Representation of downbursts and increases in lightning frequency

First, we show the general characteristics of the simulated multi-cell convective clouds. The animations in Supporting Information Movie S1 indicate that the precipitation produced by the convective clouds was generated repeatedly and lasted until the end of the simulation, which is a typical characteristic of long-lasting multi-cell convective clouds. Wind speeds exceeding 40 m s^{-1}, which corresponds to a downburst, occurred multiple times in both experiments at the time of strong precipitation exceeding 100 mm h^{-1} in addition to downdrafts exceeding 10 m s^{-1} at an altitude of 90 m which is clear the definition; 12 ft. s^{-1} at 300 ft. in Fujita and Byers (1977) (black lines in Fig. 1c, d, e, and f). In this study, the first convective cloud initiated by the warm bubble at the initial time was not considered when examining the multi-cell convective clouds triggered by a cold pool, and therefore we analyzed the results after 24 min.

In the control experiment, the lightning frequency increased and reached a local maximum at around 33.3 min (the red line in Fig. 1e), which is 14.7 min before the downburst at 48 min (the black line in Fig. 1e). The sequence of increasing lightning frequency followed by a downburst was identified as the occurrence of a preceding lightning increase corresponding to a LJ based on its definition in Section 2.3. Furthermore, strong winds exceeding 40 m s^{-1} also occurred at around 61 min and 72 min (the black line in Fig. 1e), but these downbursts were not preceded by increasing lightning frequency, corresponding to downbursts without preceding lightning increases. These results indicate successful representation of long-lasting multi-cell convection and downbursts with and without preceding lightning increases in the control experiment.

The successful representation of downbursts with and without preceding lightning increases enabled us to examine the mechanism contributing to the occurrence of a preceding lightning increase. We investigated heavy graupel particles and charge separation as precursors

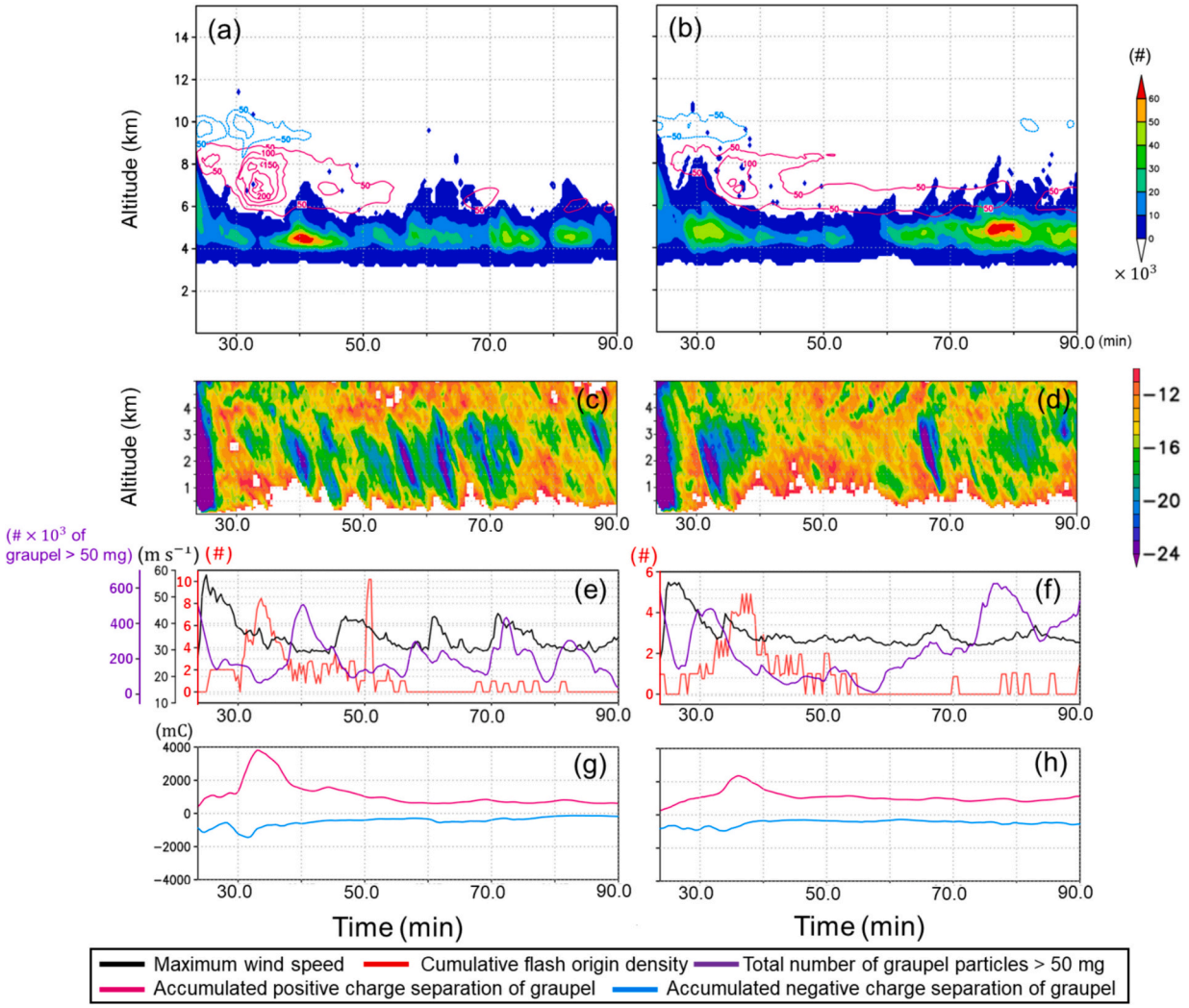

Fig. 1. (a, b) Shaded regions represent time series of accumulated number of graupel particles exceeding 50 mg (#). (c, d) Shaded regions represent time series of max downdraft exceeding 10 m s^{-1} in the model domain. The red and blue contour lines show accumulated positive and negative charge separations of graupel (mC), respectively. (e, f) Black, red, and purple lines represent maximum wind speed, cumulative flash origin density, and total number of graupel particles exceeding 50 mg within the model domain, respectively. (g, h) Pink and blue lines represent accumulated positive and negative charge separation of graupel. (a), (c) (e), and (g) show the results for the control experiment, and (b), (d), (f), and (h) show the results for the strong shear experiment. (For interpretation of the references to color in this figure legend, the reader is referred to the web version of this article.)

of downbursts and lightning, respectively. Table 1 summarizes the times of maximum charge separation (shown in Fig. 1g) and the local maximum number concentration of heavy graupel particles around the time of local maximum charge separation. In the control experiment, active charge separation occurred at around 33.3 min (the pink line in Fig. 1g), which was attributed to the positive charge separation of graupel around the height of 7 km (the pink contour lines in Fig. 1a). This active charge separation generated the large charge density of the hydrometeors and resulted in increased lightning frequency (the red line in Fig. 1e). Before the downburst at around 48 min, an increase in heavy graupel particles generated around the height of 4.5 km (the region filled with solid colors in Fig. 1a), was seen (the purple line in Fig. 1e) at 40 min, which was 8 min before the downburst. After the increase in the number of heavy graupel in the next generation cell, areas with downdrafts exceeding 20 m s^{-1} below 3 km altitude appeared (Fig. 1c, d). These results indicate that the downburst at 48 min was produced by the drag force and evaporative/sublimation cooling below the clouds caused by the heavy graupel particles.

In the strong shear experiment, the vertical distribution of the active charge separation area and the area of the active production of heavy graupel particles (Fig. 1b) were consistent with those in the control experiment (Fig. 1a), but the magnitude of the charge separation was smaller than that in the control experiment. In addition, a local maximum of heavy graupel particles (30 min) and strong wind regarded as a downburst (33 min) occurred before the increase in charge separation and lightning frequency (36.6 min) (Fig. 1b, h). This means that preceding lightning increases were absent in the strong shear experiment.

Additionally, both experiments exhibited differences in the timing and altitude of the areas where charge separation was active and where heavy graupel was existing (Fig. 1).

Table 1
Times of local maxima of charge separation amount and number of heavy graupel particles in CTL and SS experiments after 24 min from the initial time.

	Control exp.	Strong shear exp.
Charge separation	33.3 min	36.6 min
Heavy graupel particle number	40.0 min	30.0 min

3.2. Environment during preceding lightning increases and active generation of heavy graupel particles

Next, we investigate the environment during the preceding lightning increase and the active generation of heavy graupel particles to understand the differences in the physical mechanisms contributing to active charge separation and active growth of such particles, which exhibited distinct spatiotemporal characteristics in Fig. 1. To investigate these mechanisms, we focus on the mixed-phase area, where liquid and solid hydrometeors coexist in convective clouds.

Fig. 2 shows how the area in which charge separation occurs and the area with heavy graupel particles are distributed over a vertical cross-section through convective clouds. Each panel of the figure shows a snapshot at the time of either active charge separation (33.3 min in the control experiment and 36.6 min in the strong shear experiment) or active growth of heavy graupel particles (40.0 min in the control experiment and 30 min in the strong shear experiment). Fig. 2 enables consideration of the cloud microphysical and electrical properties in the mixed-phase area, together with the zoomed-in panels in Fig. 3. At the time of active charge separation in the control experiment, snow and cloud ice, graupel, and liquid water (supercooled water), marked with blue, green, and orange hatching, respectively, coexisted over the area with active charge separation at 138 km $< x <$ 145 km, 5 km $< z <$ 9 km (Figs. 2a and 3a). During this period, lightning activity increased, and no heavy graupel particles (purple hatching) were simulated in this area.

In contrast, at the time of active growth of heavy graupel particles, liquid water and graupel (shown as orange and green hatching, respectively, in Figs. 2b and 4b) coexisted at 130 km $< x <$ 132 km, 4.5 km $< z <$ 6 km, but snow and cloud ice (shown as blue hatching) were not seen over the area with production of heavy graupel particles (shown as purple hatching). The downburst at 48 min was produced by the drag force and evaporative/sublimation cooling below the clouds caused by the heavy graupel particles produced in this area (figure not shown).

The results of the strong shear experiment indicated similar trends as in the control experiment, such as the occurrence of charge separation at

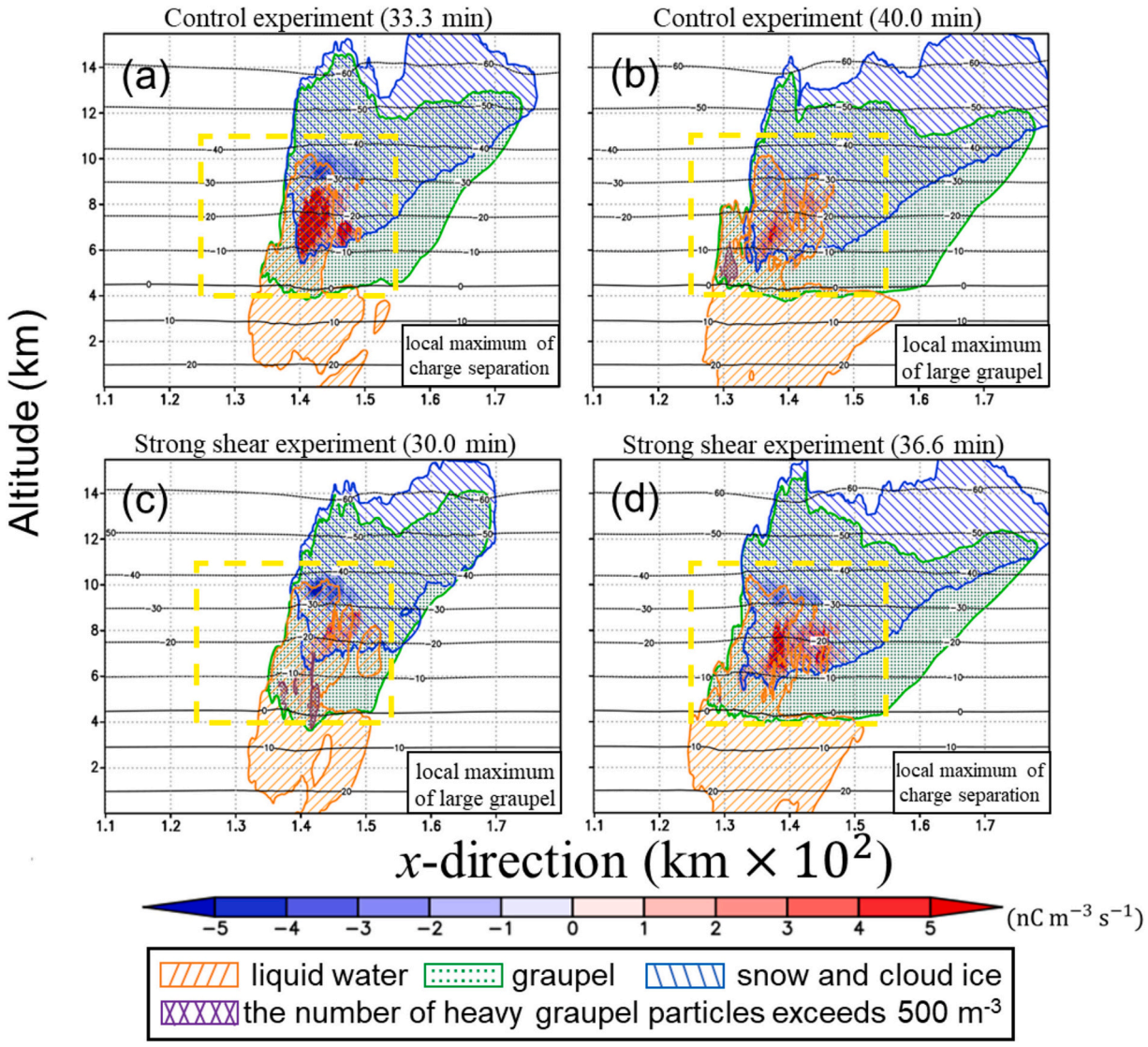

Fig. 2. The x-z cross-sections for the results or accumulated over the y gridpoints where the total hydrometeor mixing ratio exceeds 0.1 g kg^{-1} and the charge separation exceeds 0.5 nC m^{-3}, for the snapshot at (a) 33.3 min and (b) 40.0 min from the initial time of the control experiment and the snapshot at (a) 30.0 min and (b) 36.6 min in the strong shear experiment. The orange hatches, green dots, and blue hatches respectively indicate where liquid water, graupel, and snow and cloud ice exist. The purple hatches indicate areas where the number of heavy graupel particles exceeds 500 m^{-3} in accumulation. The black contours denote air temperatures (°C). A zoomed-in view of the yellow dashed box is shown in Fig. 3. (For interpretation of the references to color in this figure legend, the reader is referred to the web version of this article.)

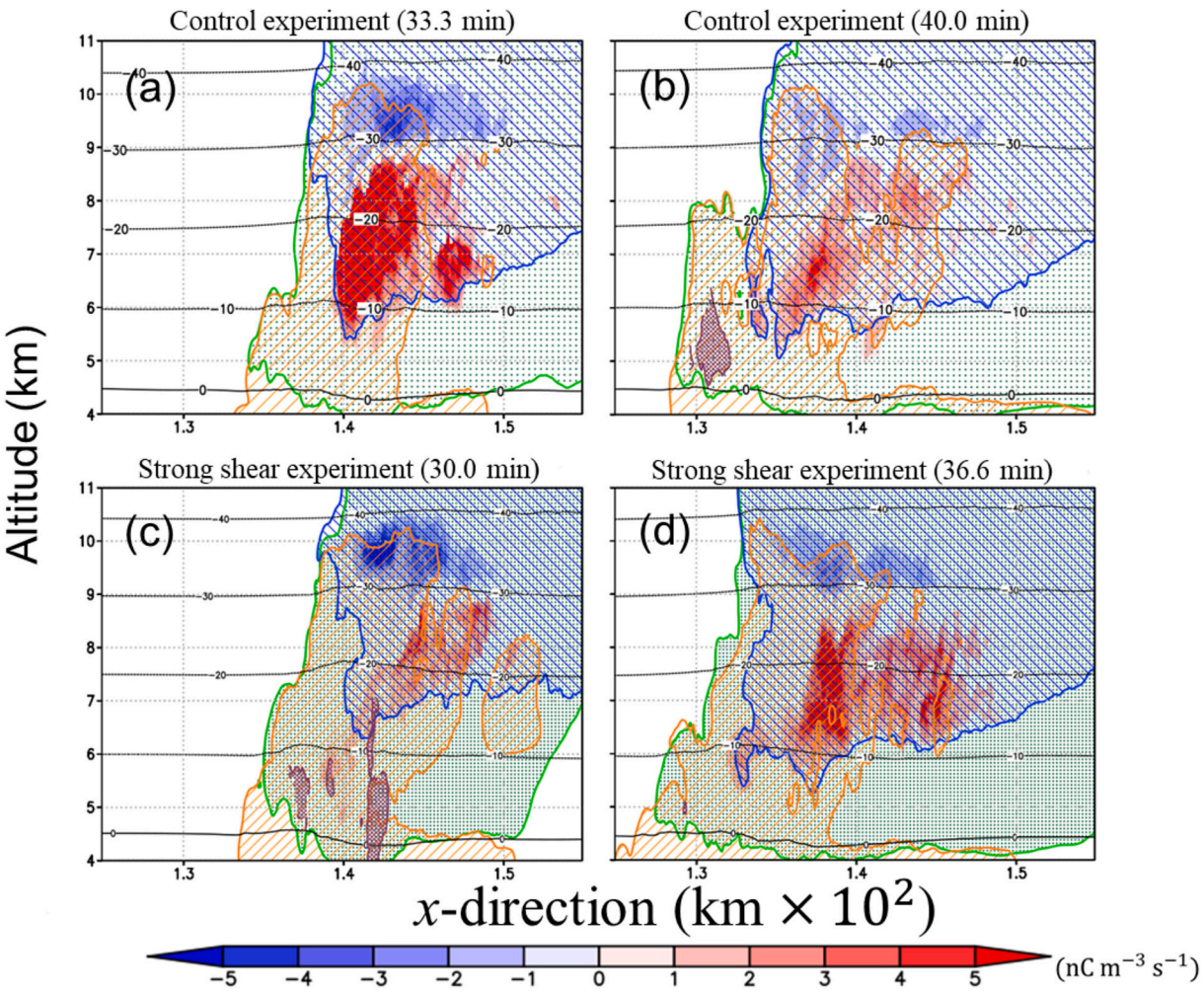

Fig. 3. Zoomed-in view of the yellow dashed box in Fig. 2. (For interpretation of the references to color in this figure legend, the reader is referred to the web version of this article.)

the area of 135 km $< x <$ 145 km, 6 km $< z <$ 9 km (Figs. 2d and 3d) and the production of heavy graupel particles at the area of 135 km $< x <$ 142 km, 4 km $< z <$ 6 km (Figs. 2c and 3c).

To examine the reason for the different characteristics at the times of active charge separation and active growth of heavy graupel particles, we analyzed the wind flow around the mixed-phase area. Fig. 4 shows vertical cross-sections of charge separation amount with streamlines at the times of active charge separation and active growth of heavy graupel particles. Fig. 4 shows the areas with heavy graupel particles (purple hatching), strong vertical velocity exceeding 25 m s^{-1} (orange hatching), and negative velocity in the x direction (green hatching). In the control experiment at the time of active charge separation (33.3 min), the area of active charge separation at 138 km $< x <$ 145 km, 5 km $< z <$ 9 km was located behind the convective area (Fig. 4a, b). In the area of active charge separation, the horizontal wind blew toward the area with active riming electrification from the rear side of the convective cloud marked by the green hatching at 140 km $< x <$ 150 km, 6 km $< z <$ 8 km in Fig. 4a, b. The horizontal wind toward this area from the rear side of the convective cell corresponds to a rear inflow jet (Fan et al., 2017; Weisman and Rotunno, 2004). Similar trends were simulated in the strong shear experiment at 140 km $< x <$ 150 km, 6 km $< z <$ 8 km marked as green hatched area in Fig. 4g, h, but the charge separation amount was small compared with that in the control experiment.

In contrast, at the time of active growth of heavy graupel particles in the control experiment, the area with heavy graupel particles coincided with the area of strong updrafts, and the horizontal wind flow from the rear side of the convection was not included in the area with heavy graupel particles. Furthermore, the area with heavy graupel particles was located around the area with strong vertical wind around $x = 130$ km in Fig. 4c, d. However, that area was distinct from the area with updrafts exceeding 25 m s^{-1} located behind it at 132 km $< x <$ 138 km. This indicates that the strong updraft at $x \approx 130$ km was a new convective cell generated by the convergence and divergence at the surface by cold pools produced by the preceding convective cell seen at 132 km $< x <$ 135 km. In the strong shear experiment, heavy graupel particles were produced in the area where $x \approx$ 142 km and 4 km $< z <$ 6 km (Fig. 4e, f).

The above analyses clarify that a horizontal wind from the rear side of the convective cell is prominent during the periods of active riming electrification. This horizontal wind from the rear side of the convective cell transported solid particles such as snow and cloud ice to the area containing graupel and liquid water, thereby generating an environment in which graupel, snow, and liquid water coexisted. In this kind of environment, snow rebounds actively during snow–graupel collisions and riming electrification occurs actively, which is supported by the −5SI and −15SI experiment using a zero-dimensional box model (Appendix D).

In contrast, in the area of active heavy-graupel growth, updrafts were dominant, and this vertical flow supplied much liquid water from the lower layers. In addition, the horizontal wind from the rear side of the convective cell was either weak or absent altogether, and few solid particles were supplied from the surroundings. In such conditions, an

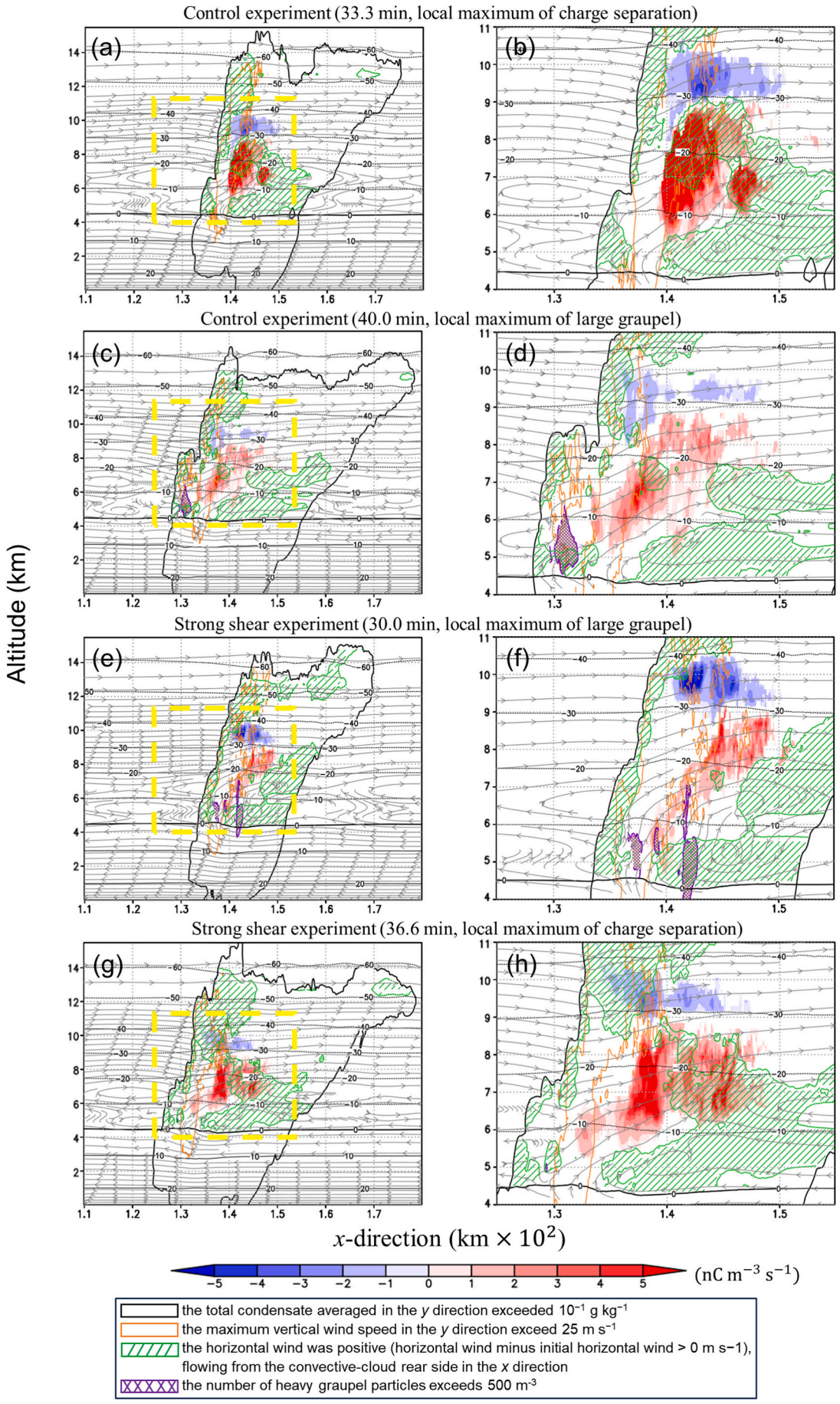

(caption on next page)

Fig. 4. Vertical cross-sections in x direction at times of local maxima of charge separation and heavy graupel particles for each experiment. The yellow dashed box in (a, c, e, g) is the area that is enlarged in (b, d, f, h). The shading represents the charge separation averaged in the y direction and indicates where it exceeded 5 nC m^{-3}. The thick black line encloses the area where the total condensate averaged in the y direction exceeded 10^{-1} g kg^{-1}, while the orange line indicates the area where the maximum vertical wind speed in the y direction exceeds 25 m s^{-1}. The gray lines with arrows are the streamlines of the wind. The green hatched area is that where the horizontal wind was positive (horizontal wind minus initial horizontal wind >0 m s^{-1}), flowing from the convective-cloud rear side in the x direction. (a–d) and (e–h) show the results from the control and strong shear experiments, respectively. (a, b) and (c, d) show the results at 33.3 min and 40 min in the control experiment, respectively, and (e, f) and (g, h) show the results at 40 min and 36.6 min in the strong shear experiment, respectively. (For interpretation of the references to color in this figure legend, the reader is referred to the web version of this article.)

environment where only graupel and liquid water coexisted was produced. Under this environment, the riming growth of graupel was active, but the riming electrification was not active because of the absence of snow and cloud ice, which is supported by the −5noSI and −15noSI experiments using a zero-dimensional box model (Appendix D). As a result, heavy graupel particles were generated actively through riming growth.

To summarize the above, the environment that was suitable for riming electrification, which leads to preceding lightning increases, was formed by the horizontal wind from the rear side of the convective cell supplying snow and cloud ice to the convective cell. Conversely, the production of heavy graupel particles contributing to downbursts grew efficiently in the environment where the riming growth of graupel was active because of the absence of solid particles and the active supply of liquid water.

To extend the above analyses to the whole period of the simulation, we investigate the horizontal wind flux of snow number concentration and the vertical flux of liquid water mass as proxies for the supply of solid particles such as snow and ice and the riming growth area. Fig. 5a–d shows the horizontal wind flux of snow number concentration against the total number of heavy graupel particles (Fig. 5a, c) and the positive charge separation of graupel (Fig. 5b, d). The heavy graupel particles existed predominantly when the horizontal flux of snow number concentration was small ($UN_S < 10^{-2}$ m^{-2} s^{-1}) (Fig. 5c). The timing of this small UN_S corresponded well with that of the generation of heavy graupel particles in the control experiment but not in the strong shear experiment (Fig. 6a–d). In contrast, charge separation of graupel occurred in the area where the horizontal flux of snow number concentration was active ($> 10^7$ m^{-2} s^{-1}) (Fig. 5b, d). The frequency of this area of large UN_S showed good correspondence with the temporal variations of positive charge separation of graupel in both experiments (Fig. 6e–h). Additionally, the negative charge separation of graupel exhibited a similar trend (not shown), although it was weaker than the positive charge separation. These results indicate that large charge separation occurred when the horizontal wind from rear side of the convective cell was strong.

Fig. 6e–h shows the vertical flux of liquid water WQ_{liq}, which contributed to the production of heavy graupel particles. These tended to form during periods when WQ_{liq} was in the range of 0–15 g $m^{-2}s^{-1}$ (e.g., Fig. 6e: 40 min; Fig. 6g: 30 min and 78 min). In contrast, charge separation of graupel occurred in the area of small WQ_{liq} (0–5 g $m^{-2}s^{-1}$) (Fig. 6f: 33 min; Fig. 6h: 36 min).

These results suggest that heavy graupel particles were produced in areas with little supply of solid particles by horizontal winds and an active supply of liquid water from the lower layers.

3.3. Formation of mixed-phase area suitable for growth of graupel and riming electrification

As described above, the control and strong shear experiments both simulated the downburst, but only the control experiment demonstrated the preceding lightning increase corresponding to the LJ event. The characteristics of convective cells exhibiting active charge separation and those producing heavy graupel particles differed in each experiment. This difference originated from the supply of solid particles to the mixed-phase area from the surroundings and lower layers, driven by wind circulation (Fig. 6). In this subsection, we discuss the conditions required for the occurrence of the preceding lightning increase. According to the analyses in Section 3.2, the horizontal wind toward the mixed-phase area corresponding to the horizontal wind from the rear side of the convective cell is a key property for active charge separation and the occurrence of the preceding lightning increase. Analyses of squall lines suggest that the rear inflow jet from the rear side of the convective cell is dominant when the convection was tilted (Weisman and Rotunno, 2004; Rotunno et al., 1988). Although the correspondence with the squall-line system in this study is not perfect, multi-cell convection was generated by the cold pool produced by the previous generation of convection. Thus, we can discuss the preceding lightning increase as LJ occurrence in multi-cell convection according to the tilting of the convection.

Fig. 7 shows the horizontal distribution of the vertical winds at altitudes of 5 km and 7 km, when active charge separation and active growth of heavy graupel particles, respectively, were seen in both experiments. At the time of active charge separation in the control experiment (33.3 min; Fig. 7a, b), the large vertical velocity around the leading edge at $z = 5$ km was located around $x = 136$ km, $y = 32$ km, which is shown as the crossing point of the dashed lines in Fig. 7a, b, and that at $z = 7$ km was distributed around $x = 140$ km, $y = 34$ km (Fig. 7b). These results indicate that the convection was tilted when charge separation was active. In contrast, the large vertical velocity was located in the same location (i.e., $x = 131$ km, $y = 32$ km) at both $z = 5$ km and 7 km when many heavy graupel particles were generated, shown as the crossing point of the dashed lines in Fig. 7c, d. Upright convection was generated at the time of the active growth of heavy graupel particles. Note that the vertical velocity at $x = 137$ km, $y = 28$ km in Fig. 7a and b and $x = 134$ km, $y = 27$ km in Fig. 7c and d was ignored because it corresponds to sustained updrafts originating from the previous convective cell rather than from the new cell at the leading edge of the cold pool.

Fig. 8 shows the convection tilt angle φ_{tilt} as defined in Section 2.4. In the control experiment (Fig. 8a), the area with active riming electrification at 140 km $< x <$ 150 km, 6 km $< z <$ 9 km predominantly exhibited tilted convection ($\varphi_{\mathrm{tilt}} < \frac{\pi}{6}$). In such a case, the horizontal transport of snow particles and riming electrification were active in the convective cell resulting in the occurrence of the preceding lightning increase. On the other hand, in the mixed-phase area with heavy-graupel production around $x = 130$ km, 4.5 km $< z <$ 6 km in Fig. 8b, most of the convection was upright ($\varphi_{\mathrm{tilt}} > \frac{5}{18}\pi$), and this led to an environment with an active supply of liquid water from the lower layers. Subsequently, heavy graupel particles contributing to downburst were produced in a newly grown upright convection cell (40.0 min).

In the strong shear experiment, the area of strong updraft was located in the area at $x = 136$ km, $y = 25.5$ km when many heavy graupel particles were generated (Fig. 7e, f), which is similar to the control experiment (Fig. 7c, d). At the time of active charge separation in the strong shear experiment, the difference in the updraft area between $z =$ 5 km and $z = 7$ km was small (Fig. 7g, h) compared with the tilting in the control experiment.

In the strong shear experiment, before the time of active charge separation, upright convection became dominant (30.0 min); this promoted the production of heavy graupel through riming (Fig. 8c), and the downburst followed it (34.3 min; Fig. 1f). Subsequently, at 36.6 min, the

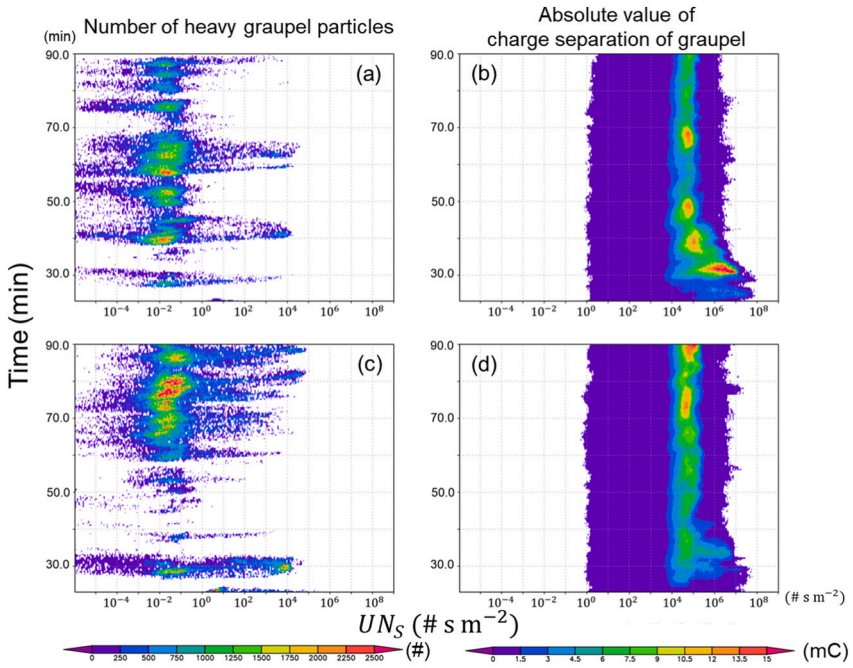

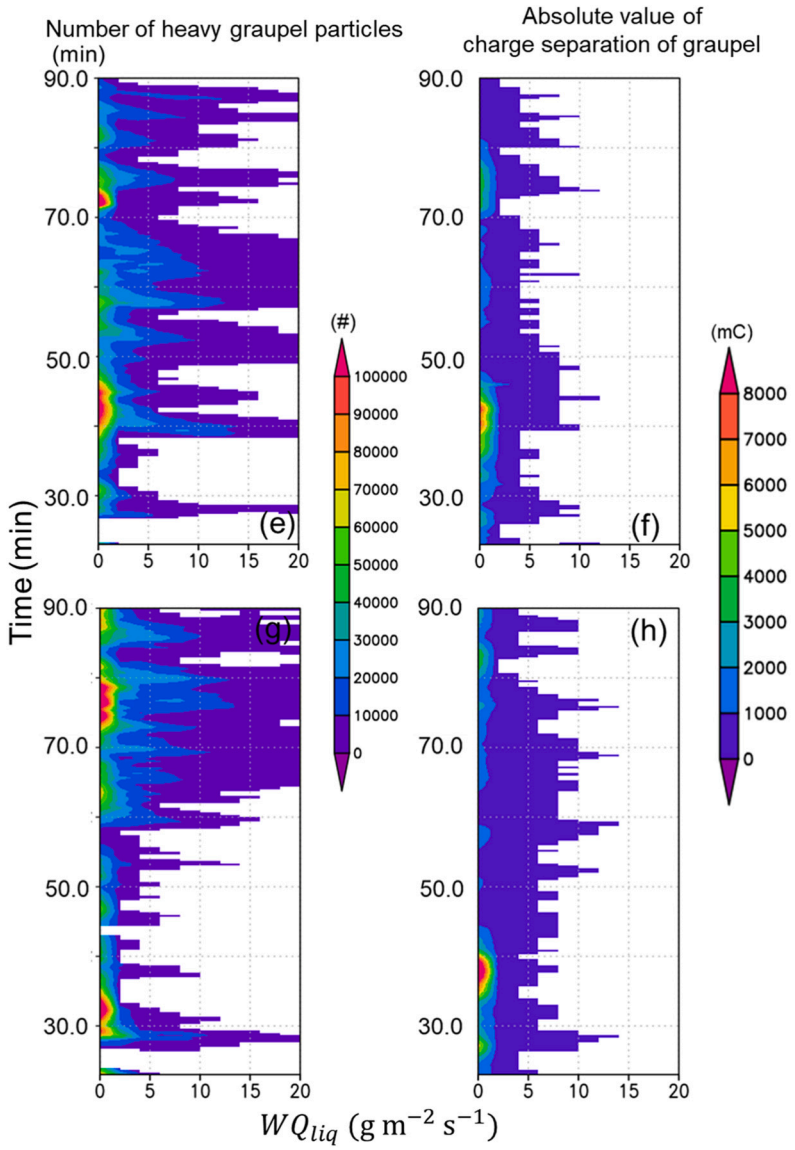

(caption on next page)

Fig. 5. Time series of distribution of summation of each variable with snow number concentration horizontal flux (m^{-2} s^{-1}) for grid cells where each variable exists after 24 min from the initial time for the control experiment (a, b) and the strong shear experiment (c, d). Panels (a) and (c) show the total values of the number of heavy graupel particles exceeding 100 mg. Panels (b) and (d) show the absolute value of charge separation of graupel exceeding 0.5 mC. (e–h) Same as (a–d) but for a time series of the distribution of vertical liquid water flux (g m^{-2} s^{-1}).

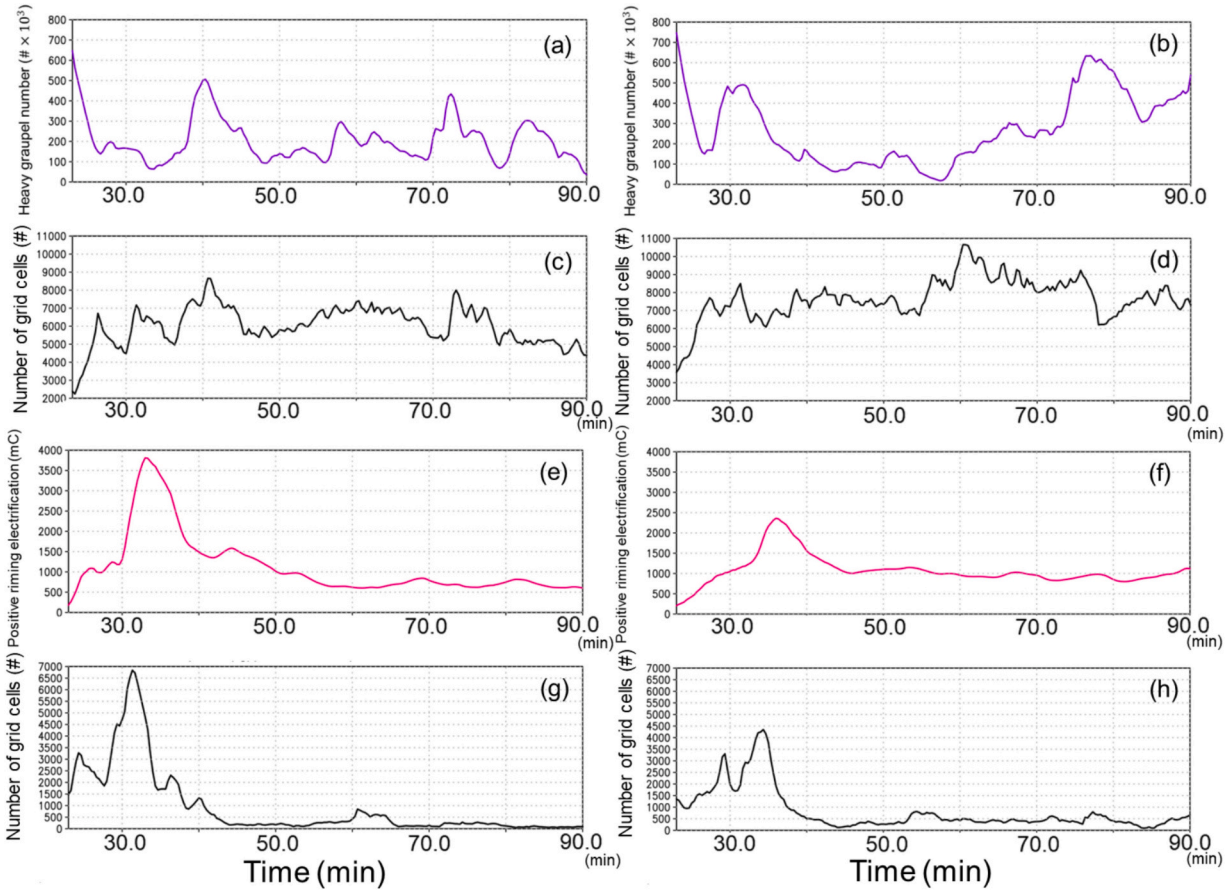

Fig. 6. Time series of quantities related to mass flux convection for the control experiment (left) and the strong shear experiment (right) after 24 min from the initial time. Panels (a) and (b) show the number of heavy graupel particles; (e) and (f) represent the positive charge separation; (c) and (d) indicate the number of grid cells where $UN_S < 10^{-2}$; and (g) and (h) correspond to the number of grid cells where $UN_S > 10^{7}$.

tilted convection led to the formation of a mixed-phase area suitable for riming electrification. As a result, charge separation attained its peak (Fig. 8d), but it did not lead to the downburst.

These results suggest that the sequence from the generation of tilted convection cells conducive to riming electrification to the growth of newly formed upright convection cells is important for active riming electrification preceding the generation of heavy graupel for LJ occurrence.

The above convection characteristics suggest that the transition to convection cell tilting is related to the LJ mechanism, and so we examined the factors contributing to this transition in the convection environment. Because all convective clouds generated in the idealized experiments that we conducted were multi-cell convective clouds, the tilting of the convection can be explained by the RKW theory introduced in Section 2.4. As reported in previous studies (Takemi, 2006; Lebo and Morrison, 2014; Rotunno et al., 1988; Weisman and Rotunno, 2004), the environment with $C/\Delta U \sim 1$ corresponds to optimal convection in the form of upright convection, while that with $C/\Delta U \gg 1$ tends to lead to tilted convection. Fig. 9 shows time series of the frequency of $C/\Delta U > 3$. In the control experiment, such an environment was seen around 26 min, which was 7 min before the time of active charge separation (33.3 min). The cold-pool intensity correlated with low-level updrafts represented a high frequency exceeding 15 m s^{-1} (black line in Fig. 9b). Therefore, tilted convection could create an environment suitable for riming electrification, leading to preceding lightning increase. Environments suitable for tilted convection with $C/\Delta U > 3$ were also observed at 45 min and 65 min (Fig. 9a). The cold-pool intensity after 47.6 min was weaker than that at 26 min (Fig. 9b), and therefore the convection was weak compared with that at 33.3 min. In such a case, the magnitude of charge separation was small and resulted in a lower lightning frequency.

The diagnosis data by $C/\Delta U$ indicated a small frequency of $C/\Delta U > 3$ at the preceding local maximum of heavy graupel particles (40.0 min) This condition suggests that an environment suitable for upright convection during 30–40 min (Fig. 9a) tended to be generated. This environment formed a continuous supply of liquid water from the lower levels with a smaller supply of solid-phase particles from the rear, and it was suitable for producing heavy graupel. Moreover, in the $C/\Delta U \sim 1$ environment, although the cold-pool intensity become weak compared with the local maximum of charge separation, multiple downbursts occurred when the convection was upright and suitable for active growth of heavy graupel in the control experiment (61 min, 72 min; Fig. 1c).

In the strong shear experiment, even when the cold-pool strength was comparable to that in the control experiment (Fig. 9b), $C/\Delta U$ tended to take smaller values because the vertical shear (ΔU) was larger. As a

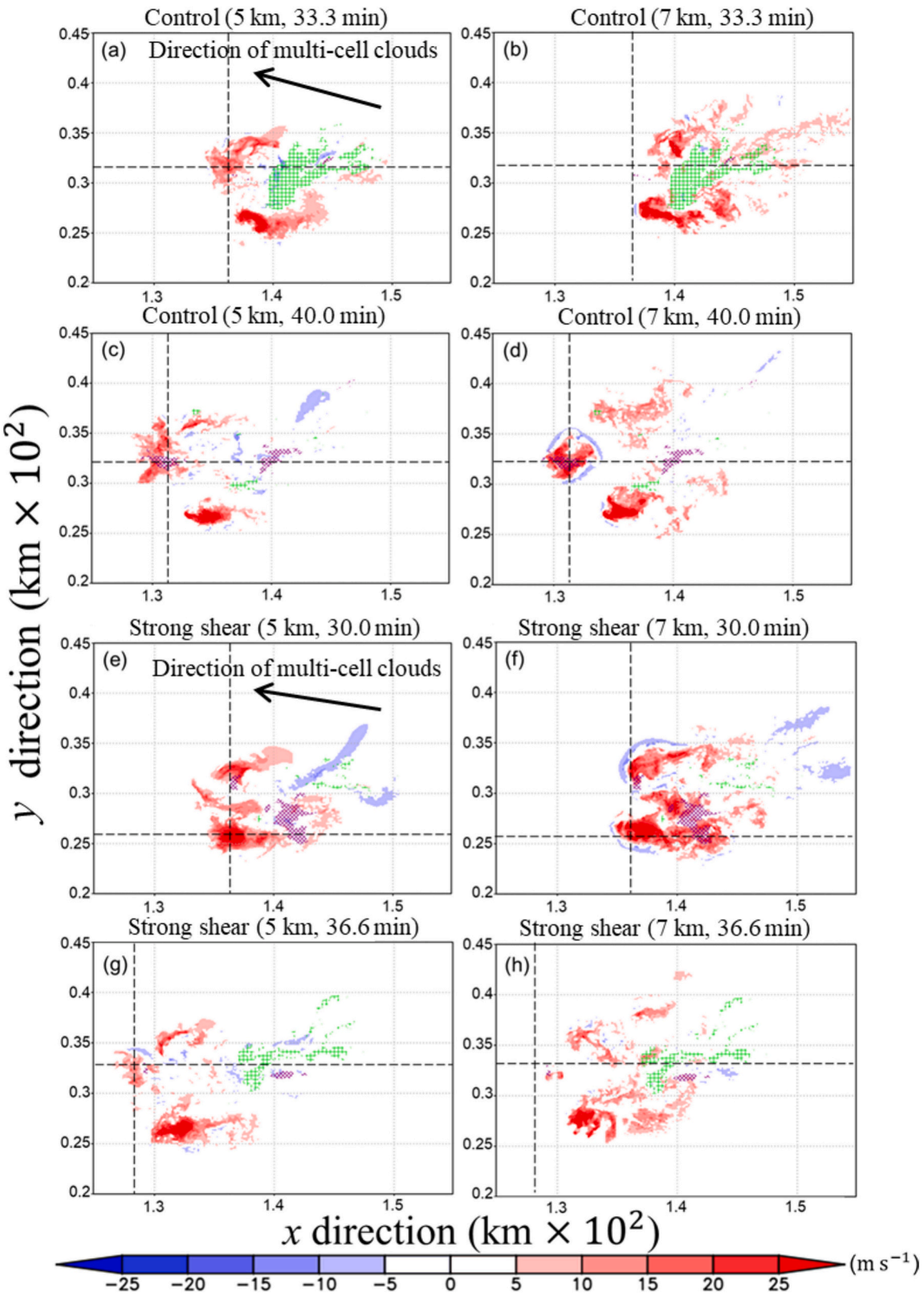

Fig. 7. Snapshot at 33.3 min for the control experiment at altitudes of 5 km (a) and 7 km (b). The red–blue shading shows vertical wind as per the reference at the bottom. Purple indicates the area where heavy graupel particles vertically integrated through the domain count >100. Green indicates the absolute value of charge separation exceeds 0.5 mC. The crossing point of the two dashed lines is the center of the area of maximum vertical velocity at z = 5 km at its time of local maximum. (c, d) Same as (a, b) but for 40.0 min. (e–h) Same as (a–d) but for the strong shear experiment. (For interpretation of the references to color in this figure legend, the reader is referred to the web version of this article.)

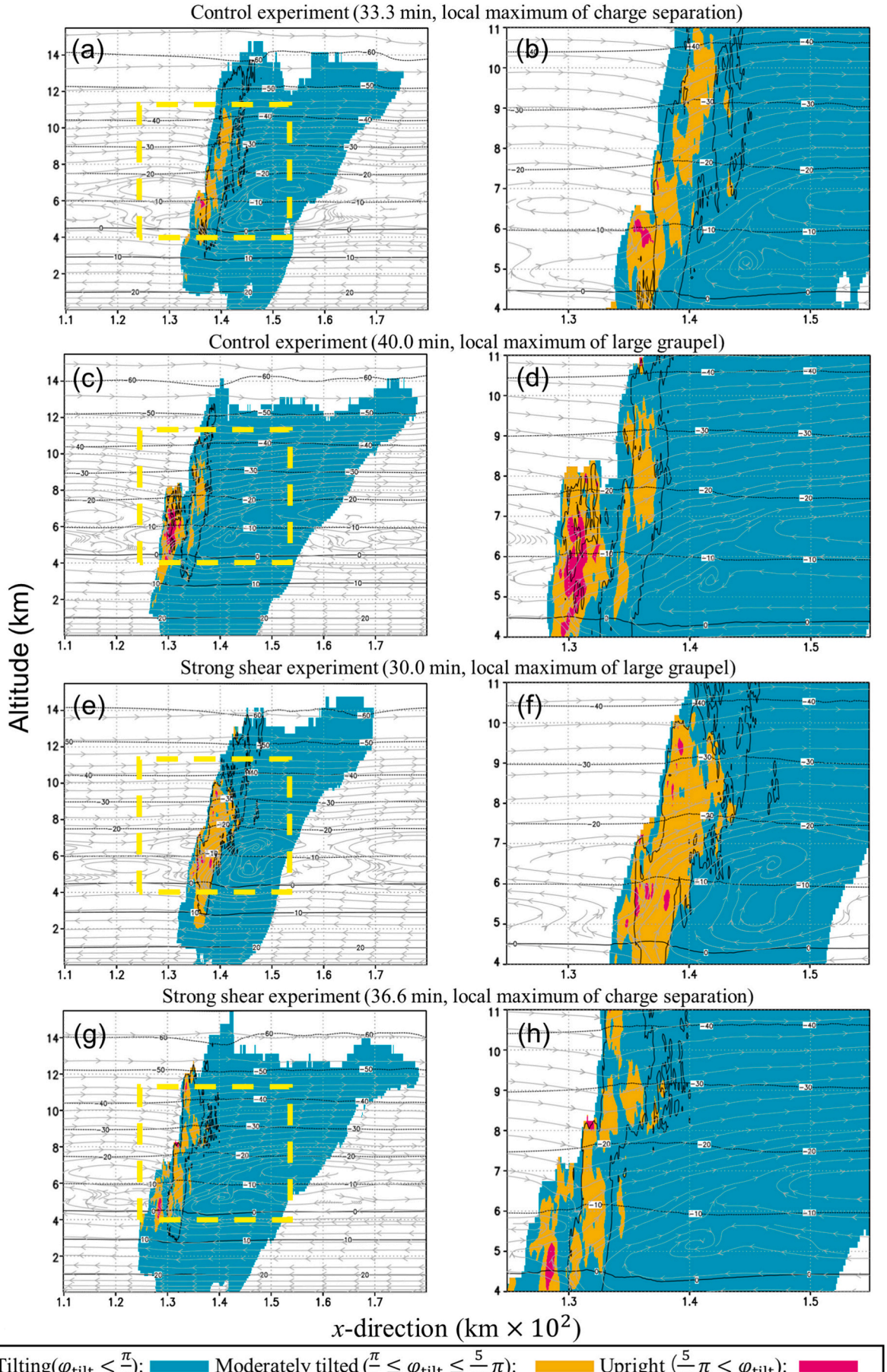

(caption on next page)

Fig. 8. Vertical distribution of wind tilting angle φ_{tilt} averaged in y direction. Blue, yellow, and red represent tilted, moderate, and upright convection, respectively, based on φ_{tilt}. The data are shown over the area where the total condensate averaged in the y direction exceeds 10 g kg^{-1}. The black lines and the gray streamlines indicate the temperature profile and the y-direction-averaged wind streamlines, respectively. (a, c) and (e, g) show the results from the control and strong shear experiments, respectively. (a) and (c) show the results at 33.3 min and 40 min in the control experiment, respectively, and (e) and (g) show the results at 40 min and 36.6 min in the strong shear experiment, respectively. The yellow dashed box in (a, c, e, g) is the area that is enlarged in (b, d, f, h). (For interpretation of the references to color in this figure legend, the reader is referred to the web version of this article.)

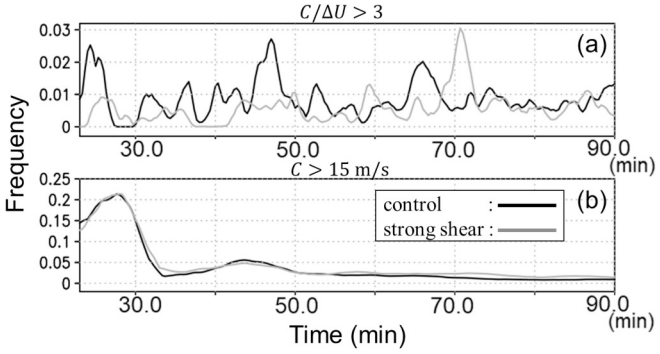

Fig. 9. Time series of normalized frequencies of (a) $C/\Delta U > 3$ and (b) $C > 15$ m s^{-1} after 24 min. The black and gray lines are the results of the control and strong shear experiments, respectively.

result, around the local maximum at 26 min simulated in the strong shear experiment, the frequency of $C/\Delta U > 3$ (Fig. 9a) was relatively lower, and this feature could form an environment suitable for upright rather than tilted convection. Consequently, this upright convection promoted the active growth of heavy graupel particles starting at 30.0 min.

Based on the relationship between cold-pool intensity and vertical wind shear, we propose the following conditions for the occurrence of the preceding lightning increase. When a convective cell is tilted and sufficient cold-pool intensity is generated, an environment suitable for charge separation is formed and leads to increased lightning activity. If the subsequently generated convective cells are upright, then heavy graupel particles are produced therein, leading to downbursts, and this transition leads to the preceding lightning increase. In contrast, in cases where only upright convection occurs, while heavy-graupel production is more likely, downbursts can still occur. However, the occurrence of riming electrification is less likely, implying that a LJ may not occur. In addition, when the cold pool is weak, the tilted convection does not lead directly to the active charge separation required for the increase of lightning.

4. Discussion

The model simulated well a preceding lightning increase corresponding to a LJ characterized by an increase in the lightning flash rate approximately 15 min preceding a downburst. In contrast, a downburst occurred 3 min before the increase of the lightning and no preceding lightning increase occurred when the vertical wind shear was larger. Since these experiments share the same conditions except for the initial wind field, the differences in cold pool intensity driven by the initial warm bubble were also small. Therefore, the differences in these results suggest that changes in the wind environment play a fundamental role in the formation of multi-cell convective clouds.

When the lightning increased before a downburst, the convection was tilted because of the strong updraft caused by the strong cold pool, and a horizontal wind from the rear side of the convective cell blew. This supplied abundant solid particles such as snow and ice for the mixed-phase area in the convective cell. This supply of solid precipitation particles produced an environment in which graupel, liquid water, and snow and ice coexisted, which was suitable for charge separation by the riming electrification mechanism.

In contrast, when convective clouds with no preceding lightning increase were produced, upright convection was generated, and the supply of solid precipitation particles by the horizontal wind from the rear side of the convective cell was prohibited. In such conditions, liquid (supercooled) water was supplied for the mixed-phase area of the convective cell, and an environment with coexisting graupel and liquid water but without snow and ice was produced. In such an environment, riming electrification was prohibited, and the graupel particles grew large via the riming process and resulted in a downburst. This characteristic suggests that an environment with a limited supply of solid particles enhances the growth of heavy graupel.

The conditions required for the occurrence of the preceding lightning increase were examined by analyzing the transition of cloud microphysical properties, the tilting of convection, and the strength of the cold pool according to the RKW theory. Our analysis clarified that the transition from a tilted convection cell triggered by a strong cold pool to an upright convection cell is required for the occurrence of the preceding lightning increase. In other cases, the upright convective cell leads to a downburst before the intensification of lightning activity because riming electrification becomes less active during upright convection. In such cases, a downburst occurs without a preceding lightning increase. The former is relevant to charge separation, and the latter is associated with the generation of heavy graupel particles. When the cold pool is weak, so is the convection, and therefore the charge separation required for the increase in lightning is not active, but a downburst occurs, nevertheless.

The difference between convective cells of different generations with active riming and those with active riming electrification is consistent with observations and laboratory experiments on the growth environment of wet-growth hail and the characteristics of charge separation. Emersic et al. (2011) reported that during the early stages of thunderstorm development, lightning tends to avoid wet-growth regions of hail. Jayaratne and Saunders (2016) conducted laboratory experiments using ice crystals and an icing cylindrical rod simulating riming hail to observe charge separation by riming electrification, and they found that when the ice crystals and simulated hail collided, little charge separation occurred in the wet-growth regions of the simulated hail.

The hypothesis regarding the conditions for the increase in lightning activity preceding downbursts in multi-cell convective clouds is supported by previous studies. Several studies have reported that not only extremely strong updrafts but also moderate ones can enhance the growth of graupel such as hail (Jewell and Brimelow, 2009; Lin and Kumjian, 2022; Nixon et al., 2023). Furthermore, the characteristics of the environment with active riming electrification are consistent with previous findings that environments with vortices and turbulence generated by rear inflow jets derived from tilted convection, are conducive to lightning occurrence referred to as a “lightning bubble”(Ushio et al., 2003; Salinas et al., 2022). The insights gained from the present study align with findings from previous numerical and observational research on the tilting of convective clouds conducive to lightning activity (Gharaylou et al., 2020) and on the characteristics of low-level wind shear features that inhibit production of heavy graupel particles (Nelson, 1987; Kumjian and Ryzhkov, 2008; Dennis and Kumjian, 2017). Furthermore, the increase in lightning activity during rearward advection into convective regions caused by the merging of convective cells (Lu et al., 2021, 2022) is consistent with our hypothesis that charge separation is enhanced by the supply of solid-phase particles from the rear. This alignment implies that such observations can be

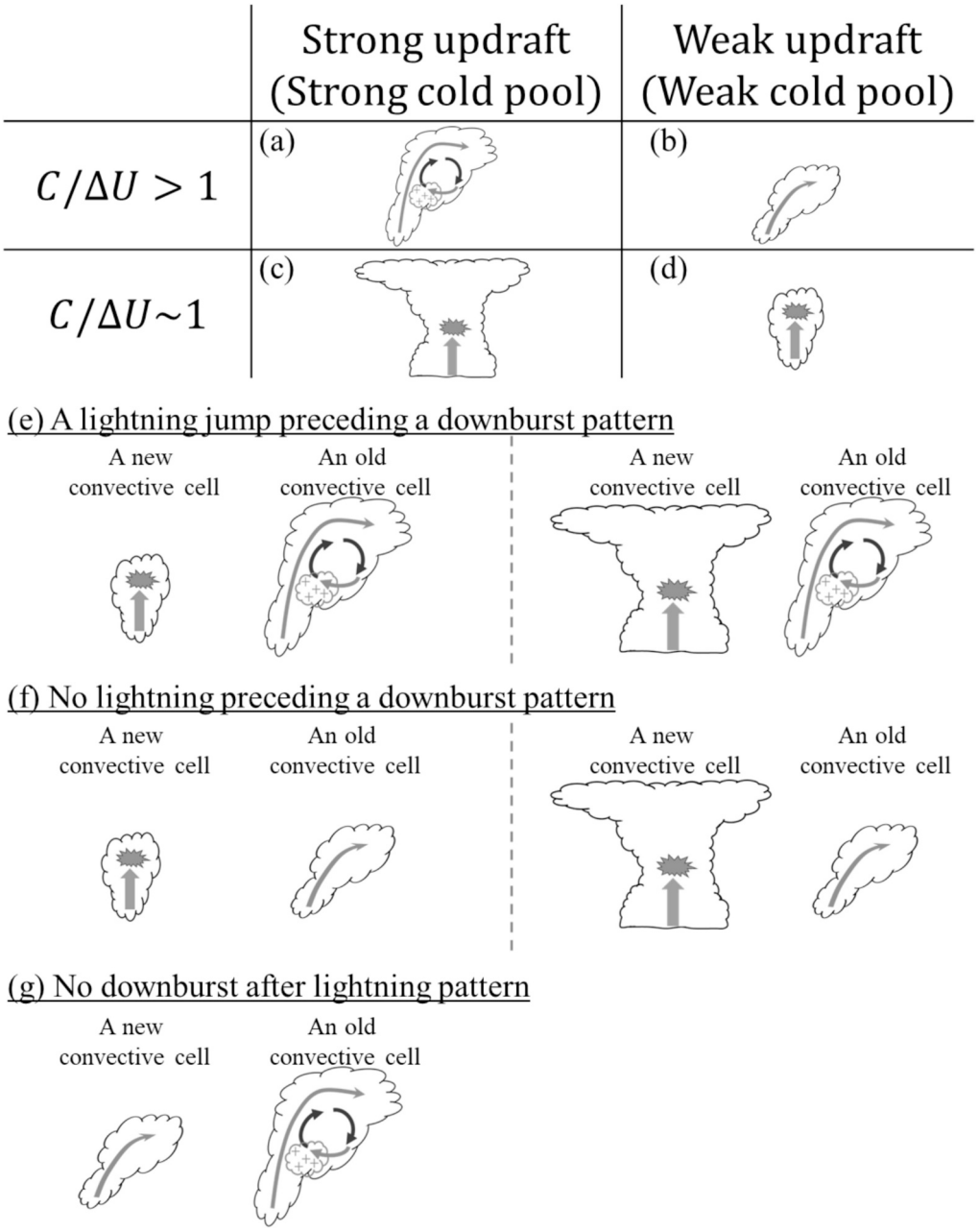

Fig. 10. Schematics of convective cells determined by $C/\Delta U$ and updrafts: (a) tilted convection with strong updrafts; (b) tilted convection with relatively weak updrafts; (c) upright convection with strong updrafts; and (d) upright convection with relatively weak updrafts. (e–g) schematic diagram of whether an LJ occurs preceding a downburst, driven by the regeneration of individual convective cells determined by $C/\Delta U$ and updrafts. (e) Representation of a pattern in which an LJ occurs preceding a downburst; (f) a downburst occurs without preceding lightning activity; and (g) lightning occurs without resulting in a downburst.

valuable for validating our hypothesis.

5. Conclusion

This study aimed to propose possible mechanisms and conditions necessary for LJs in multi-cell convection by focusing on riming growth and riming electrification, which are good indicators of downburst and lightning, respectively. To achieve this, we conducted idealized experiments focused on multi-cell convective clouds, using a meteorological model coupled with a bulk lightning model that explicitly calculates lightning and graupel growth processes. The experiments were conducted using sounding data from a case of multiple downburst events with lightning.

In this study, through the analysis focused on graupel in a mixed-phase area, the convective cell can be categorized into the following four patterns as illustrated schematically in Fig. 10 according to the relationship between the strength of the cold pool (C) and the vertical shear of the horizontal wind (DU).

1. When $C/\Delta U \gg 1$ and the cold pool is strong, the convection tends to tilt and updrafts are strong. This environment forms a tilted convective cell with an abundant supply of solid particles by the horizontal wind from the rear side of the convective cell corresponding to a rear inflow jet, contributing to riming electrification (Fig. 10a).
2. When $C/\Delta U \gg 1$ and the cold pool is weak, the convection tends to tilt and updrafts are relatively weak. This environment forms a convective cell with a limited supply of solid particles contributing to

riming electrification. In this environment, the lightning is less active, as is the growth of heavy graupel particles (Fig. 10b).

3. When $C/\Delta U \sim 1$ and the cold pool is strong, the convection tends to be upright and updrafts are strong. This environment forms a convective cell supplying abundant liquid water from the lower layers and few solid particles contributing to the production of heavy graupel particles (Fig. 10c).
4. When $C/\Delta U \sim 1$ and the cold pool is weak, the convection tends to be upright and updrafts are relatively weak. This environment forms a convective cell supplying liquid water from the lower layer and few solid particles. Then if liquid water is supplied sufficiently to grow graupel particles by riming, heavy graupel particles can be produced and result in a downburst (Fig. 10d).

From our analyses, we suggest that an LJ occurs when a convective cell transitions in the sequence of Fig. 10a to c or d from one convection to the next in multi-cell convection (Fig. 10e). In this context, LJ events do not always occur in all multi-cell convective clouds; rather, an LJ develops provided that certain critical conditions are satisfied (Fig. 10e–g). Additionally, LJ events originating from the transition of convective cells are not expected in isolated convective clouds; this is consistent with the observation that multi-cell convective clouds are associated more with LJ events than are isolated convective clouds (Rigo and Farnell, 2022).

While the transitions in the mixed-phase area present in this study require verification through observations of both graupel and snow in mixed-phase clouds, indirect validation could be possible by observing the reflectivity core and wind circulations within convective clouds. This highlights the need for further research and combined observations of hydrometeor identification and wind velocity field to fully understand the complexities of mixed-phase transitions in convective clouds. In addition, treating LJs as a more-sophisticated index of weather warnings (e.g., Schultz et al., 2009) requires an understanding of the lead time preceding LJ occurrence, which still poses a challenge.

CRediT authorship contribution statement

Makoto Kondo: Writing – review & editing, Writing – original draft, Visualization, Validation, Methodology, Investigation, Funding acquisition, Formal analysis, Data curation, Conceptualization. **Yousuke Sato:** Writing – review & editing, Writing – original draft, Supervision, Software, Resources, Project administration, Funding acquisition, Conceptualization.

Declaration of competing interest

The authors declare that they have no known competing financial interests or personal relationships that could have appeared to influence the work reported in this paper.

Acknowledgments

This work was supported by JSPS KAKENHI (Grant Numbers JP20H04196, JP20H05729, JP23KJ0037, and 24H00257), the Moonshot R&D program of the JST (Grant Number JPMJMS2286), the Support Program for Next Generation Supercomputer of the Information Initiative Center of Hokkaido University, the Cooperative Research Activities of Collaborative Use of Computing Facility (JURCAOSCFS23-02) of the Atmosphere and Ocean Research Institute, the University of Tokyo, the SECOM Science and Technology Foundation, and the Research Field of Hokkaido Weather Forecast and Technology Development (endowed by the Hokkaido Weather Technology Center Co., Ltd.). The SCALE library was developed by Team-SCALE of the RIKEN Center for Computational Sciences. We would like to thank ThinkSCIENCE for English language editing. We also thank Prof. Niino of the University of Tokyo for supplying the sounding data and for his useful comments.

Appendix A. Initial profiles for idealized experiment

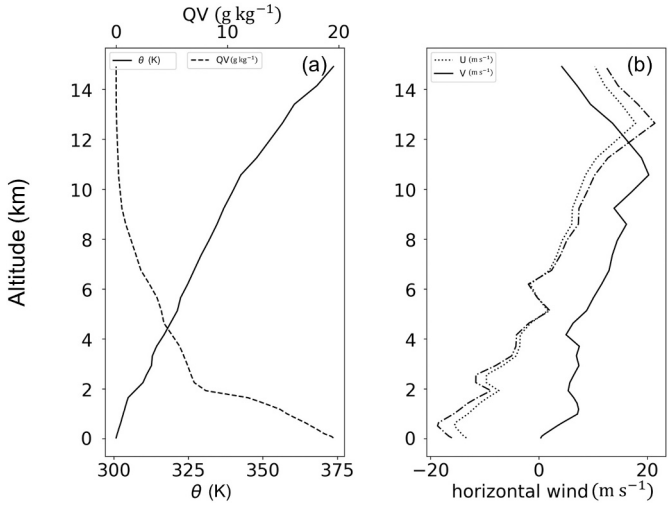

Fig. A1. Initial profiles for idealized experiment: (a) potential temperature (solid line) and vapor mixing ratio (dashed line); (b) horizontal wind speed in x direction (dotted line) and y direction (solid line), and horizontal wind speed in x direction in strong shear (SS) experiment (dash-dotted line).

Appendix B. Summarized used schemes for numerical experiment

Table B1
All schemes used in numerical simulation of the CTL experiment and the SS experiment.

Physics	Scheme	Reference
Lightning	Bulk lightning model	Sato et al. (2019)
Cloud microphysics	2-Moment bulk microphysics scheme	Seiki and Nakajima (2014)
Vertical flux by turbulence	Smagorinsky-type sub-grid model	Scotti et al. (1993), Smagorinsky (1963), Brown et al. (1994)
Horizontal flux by turbulence	Mellor–Yamada-type planetary boundary layer scheme	Nakanishi and Niino (2004, 2009)

Appendix C. The used equations of Miyamoto (2021) and Takemi (2006) in this study

To trigger convection, a potential-temperature perturbation θ' was defined by Eq. (C1) based on Miyamoto (2021).

$$\theta'(x,y,z) = \begin{cases} \theta_{wb}\cos\left(\frac{\pi}{2}\sqrt{l_{wbh}+l_{wbv}}\right), \text{for } \sqrt{l_{wbh}+l_{wbv}} \le 1.0, \\ 0, \text{for } 1.0 < \sqrt{l_{wbh}+l_{wbv}}, \end{cases} \tag{C1}$$

where θ_{wb} is the amplitude of θ', and we have $l_{wbh} = (r_{wbh}/r_{wbv})^2$ and $l_{wbv} = (r_{wbz}/r_{wbh})^2$, where r_{wbh} and r_{wbz} are the horizontal and vertical distances from the bubble center, respectively. In both experiments, we set $\theta_{wb} = 4$ K, $r_{wbh} = 4$ km, and $r_{wbz} = 1$ km.

We calculated $C/\Delta U$ for our results to examine suitable environments for tilted or upright convection, with C, B, and ΔU defined in Takemi (2006) as follows:

$$C^2 = \int_0^H (-B)dz, \tag{C2}$$

$$B = g\left(\frac{\theta-\overline{\theta}}{\overline{\theta}} + \left(\frac{R_v}{R_d}\right)(q_v - \overline{q_v}) - q_{hyd}\right), \tag{C3}$$

$$\Delta U = U_{horiz,z=H} - U_{horiz,z=0}, \tag{C4}$$

where g is the acceleration due to gravity, θ is the potential temperature, q_v is the water vapor mixing ratio, q_{hyd} is the total hydrometeor mass mixing ratio defined as the sum for all hydrometeor categories, B is buoyancy, R_d is the gas constant for dry air, R_v is the gas constant for water vapor, and H is the cold pool thickness. H = 5 km, as referenced in Takemi (2006). Overbars indicate the model's base state defined as domain-averaged variables.

Appendix D. Zero-dimensional collection process and box model

To understand the characteristics of the environments suitable for the growth of graupel by riming and charge separation by riming electrification within mixed-phase areas, we conducted zero-dimensional collection experiments using a zero-dimensional box model. The model was constructed by using only the scheme for calculating the collection processes, including riming and aggregation of the cloud microphysics scheme used in this study (Seiki and Nakajima, 2014). Using this model, the variation of each hydrometeor's category can be calculated by only the collection process.

The initial values for the experiments were created from the output of the zero-dimensional box model in a grid box within the mixed-phase area, and the output values were adjusted to simple ones to make the sensitivity experiments easier. As given in Table D1, the output values of density and the mass mixing ratio and number concentration of graupel, snow, and cloud ice were those at $x = 141$ km, $y = 31$ km, and $z = 7$ km at the time of active charge separation in the control experiment (at 33.3 min) to test the rebound between graupel and snow as a means of riming electrification. The output values of the other variables were those at $x = 141$ km, $y = 38$ km, and $z = 5000$ m at the time of active production of heavy graupel in the control experiment (at 40.0 min) to test the riming growth. Note that the influence of the selection of density and pressure on these sensitivity experiments was negligible (figure not shown). The sensitivity experiments were conducted by sweeping the temperature and the number concentration of snow/ice, and for this we selected the temperature range of active charge separation (−15 °C) in Fig. 3a and active graupel production (−5 °C) in Fig. 3b in Section 3.2. Additionally, experiments were conducted to investigate the influence of solid-particle supply on charge separation and graupel growth. For the experiments, the values for ice and snow were set to zero or present, and the values for rain and cloud water were set to fixed values. The experiments were named as given in Table D2.

Fig. D1 shows the time series of each variable. For the graupel mixing ratio (Fig. D1a), its rate of increase was temperature dependent, but the graupel mixing ratio increasing with time was a common feature of all four experiments. Meanwhile, the mean graupel weight increased when the number concentration decreased and vice versa (Fig. D1b and c). When ice and snow were present (i.e., experiments −5SI and −15SI), particles rebounded actively during graupel–snow collisions when the temperature was low (Fig. D1d). In addition, the number of graupel particles decreased more effectively in the experiments with higher temperature (Fig. D1e), suggesting that the smaller number of graupel particles resulted in fewer particles rebounded by collisions in warmer temperatures. Thus, collisions and rebounds between graupel and snow, which are critical for riming electrification, become more active at low temperatures because of the low sticking efficiency.

In contrast, when the temperature was high, the number of rebounding particles was small (Fig. D1d). In such conditions, the graupel particles tend to stick more effectively, and so they become heavy (Fig. D1c) and their number concentration becomes small (Fig. D1b, e).

Without snow and ice (i.e., experiments −5noSI and −15noSI), the graupel number and weight were small and large, respectively (Fig. D1b, c), and the graupel easily became heavy (Fig. D1c).

The results outlined above suggest that heavy graupel particles tend to be produced when the temperature is higher and the supply of snow particles is limited, while lower temperature and active supply of ice and snow particles result in increased charge separation.

Table D1
Initial values for sensitivity experiments using zero-dimensional collection process.

Variable	Value	Unit
Temperature	−15/−5	°C
Density (ρ)	0.708	kg m^{-3}
Pressure	548	hPa
ρQ_g	6.372×10^{-3}	kg m^{-3}
ρQ_s	1.070×10^{-5}/0.0	kg m^{-3}
ρQ_i	4.404×10^{-5}/0.0	kg m^{-3}
ρQ_r	2.266×10^{-3}	kg m^{-3}
ρQ_c	3.394×10^{-3}	kg m^{-3}
N_g	5133.0	m^{-3}
N_s	4248.0/0.0	m^{-3}
N_i	62,304/0.0	m^{-3}
N_r	19,824.0	m^{-3}
N_c	198,240.0	m^{-3}

Table D2
Names of all zero-dimensional experiments.

	Snow and cloud ice	No snow and cloud ice
High temperature (−5 °C)	−5SI	−5noSI
Low temperature (−15 °C)	−15SI	−15noSI

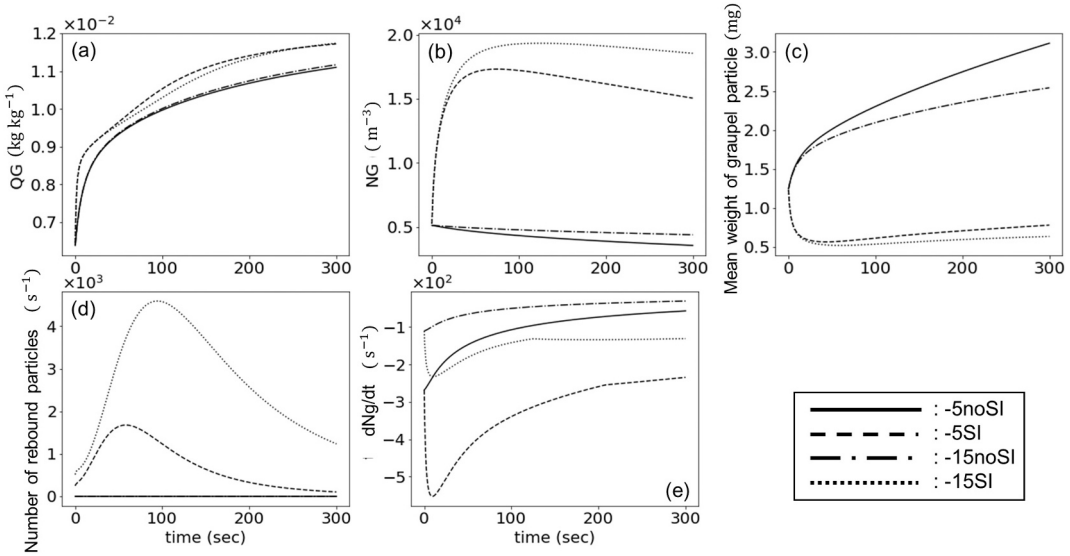

Fig. D1. Time series of each variable in experiments involving zero-dimensional collection process: (a) graupel mass mixing ratio; (b) number of graupel particles; (c) mean weight of graupel particles; (d) number of rebounding particles after collision between graupel and snow in unit time; (e) variation of graupel collision number. Solid, dashed, dash-dotted, and dotted lines represent the experiments with no snow/ice particles at −5 °C (experiment −5noSI), snow/ice particles at −5 °C (experiment −5SI), no snow/ice particles at −5 °C (experiment −15noSI), and snow/ice particles at −15 °C (experiment −15SI), respectively.

Appendix E. Supplementary data

Supplementary data to this article can be found online at https://doi.org/10.1016/j.atmosres.2025.108203.

Data availability

Data will be made available on request.

References

Barthe, C., Chong, M., Pinty, J.-P., Bovalo, C., Escobar, J., 2012. CELLS v1.0: updated and parallelized version of an electrical scheme to simulate multiple electrified clouds and flashes over large domains. In: Geoscientific Model Development. Katlenburg-, Lindau, p. 5.

Brdar, S., Seifert, A., 2018. McSnow: a Monte-Carlo particle model for riming and aggregation of ice particles in a multidimensional microphysical phase space. J Adv Model Earth Syst 10, 187–206. https://doi.org/10.1002/2017MS001167.
Brown, A.R., Derbyshire, S.H., Mason, P.J., 1994. Large-eddy simulation of stable atmospheric boundary layers with a revised stochastic subgrid model. Q. J. Roy. Meteorol. Soc. 120, 1485–1512.
Chen, Z., Qie, X., Yair, Y., Liu, D., Xiao, X., Wang, D., Yuan, S., 2020. Electrical evolution of a rapidly developing MCS during its vigorous vertical growth phase. Atmos. Res. 246, 105201. https://doi.org/10.1016/J.ATMOSRES.2020.105201.
Deierling, W., Petersen, W.A., Latham, J., Ellis, S., Christian, H.J., 2008. The relationship between lightning activity and ice fluxes in thunderstorms. J. Geophys. Res. Atmos. 113, 15210. https://doi.org/10.1029/2007JD009700.
Dennis, E.J., Kumjian, M.R., 2017. The impact of vertical wind shear on hail growth in simulated supercells. J. Atmos. Sci. 74, 641–663. https://doi.org/10.1175/JAS-D-16-0066.1.
Dolan, B., Rutledge, S.A., Lim, S., Chandrasekar, V., Thurai, M., 2013. A robust C-band hydrometeor identification algorithm and application to a long-term polarimetric radar dataset. Journal of Applied Meteorology and Climatology 52 (9), 2162–2186. https://doi.org/10.1175/JAMC-D-12-0275.1.
Dye, J.E., Jones, J.J., Winn, W.P., Cerni, T.A., Gardiner, B., Lamb, D., Pitter, R.L., Hallett, J., Saunders, C.P.R., 1986. Early electrification and precipitation development in a small, isolated Montana cumulonimbus. J. Geophys. Res. Atmos. 91, 1231–1247. https://doi.org/10.1029/JD091ID01P01231.
Emersic, C., Heinselman, P.L., MacGorman, D.R., Bruning, E.C., 2011. Lightning activity in a hail-producing storm observed with phased-array radar. Mon. Weather Rev. 139, 1809–1825. https://doi.org/10.1175/2010MWR3574.1.
Erdmann, F., Poelman, D.R., 2023. Automated Lightning Jump (LJ) detection from geostationary satellite data. J. Appl. Meteorol. Climatol. 62 (11), 1573–1590. https://doi.org/10.1175/JAMC-D-22-0144.1.
Fan, J., Han, B., Varble, A., Morrison, H., North, K., Kollias, P., Chen, B., Dong, X., Giangrande, S.E., Khain, A., Lin, Y., Mansell, E., Milbrandt, J.A., Stenz, R., Thompson, G., Wang, Y., 2017. Cloud-resolving model intercomparison of an MC3E squall line case: part I—convective updrafts. J. Geophys. Res. Atmos. 122 (17), 9351–9378. https://doi.org/10.1002/2017JD026622.
Farnell, C., Rigo, T., 2020. The lightning jump algorithm for nowcasting convective rainfall in Catalonia. Atmosphere 11, 397. https://doi.org/10.3390/ATMOS11040397.
Farnell, C., Rigo, T., Pineda, N., 2017. Lightning jump as a nowcast predictor: application to severe weather events in Catalonia. Atmos. Res. 183, 130–141. https://doi.org/10.1016/J.ATMOSRES.2016.08.021.
Fierro, A.O., Mansell, E.R., Macgorman, D.R., Ziegler, C.L., 2013. The implementation of an explicit charging and discharge lightning scheme within the WRF-ARW model: benchmark simulations of a continental squall line, a tropical cyclone, and a winter storm. Mon. Weather Rev. 141 (7), 2390–2415. https://doi.org/10.1175/MWR-D-12-00278.1.
Fujita, T.T., 1985. The downburst: microburst and macroburst. In: University of Chicago SMRP Research Paper, 210, 122 pp.
Fujita, 1992. The mystery of severe storms. In: WRL Research Paper, 239. University of Chicago, 298 pp.
Fujita, T.T., Byers, H.R., 1977. Spearhead echo and downburst in the crash of an airliner. Mon. Wea. Rev. 105, 129–146. https://doi.org/10.1175/1520-0493(1977)105<0129:SEADIT>2.0.CO;2.
Gatlin, P.N., Goodman, S.J., 2010. A total lightning trending algorithm to identify severe thunderstorms. J. Atmos. Oceanic Tech. 27, 3–22. https://doi.org/10.1175/2009JTECHA1286.1.
Gharaylou, M., Pegahfar, N., Farahani, M.M., 2020. Influence of tilting effect on charge structure and lightning flash density in two different convective environments. Meteorol. Appl. 27 (5), e1957. https://doi.org/10.1002/MET.1957.
Goodman, S.J., Buechler, D.E., Wright, P.D., Rust, W.D., 1988. Lightning and precipitation history of a microburst-producing storm. Geophys. Res. Lett. 15 (11), 1185–1188. https://doi.org/10.1029/GL015I011P01185.
Goodman, S.J., Blakeslee, R., Christian, H., Koshak, W., Bailey, J., Hall, J., McCaul, E., Buechler, D., Darden, C., Burks, J., Bradshaw, T., Gatlin, P., 2005. The North Alabama Lightning Mapping Array: recent severe storm observations and future prospects. Atmos. Res. 76, 423–437. https://doi.org/10.1016/J.ATMOSRES.2004.11.035.
Guo, X., Niino, H., Guo, X., Kimura, R., 1999. Numerical Modeling on a Hazardous Microburst-producing Hailstorm. Science Press.
Hjelmfelt, M.R., 1988. Structure and life cycle of microburst outflows observed in Colorado. J. Appl. Meteorol. 27, 900–927. https://doi.org/10.1175/1520-0450(1988)027<0900:SALCOM>2.0.CO;2.
Jayaratne, E.R., Saunders, C.P.R., 2016. The interaction of ice crystals with hailstones in wet growth and its possible role in thunderstorm electrification. Q. J. Roy. Meteorol. Soc. 142, 1809–1815. https://doi.org/10.1002/QJ.2777.
Jewell, R., Brimelow, J., 2009. Evaluation of Alberta hail growth model using severe hail proximity soundings from the United States. Weather and Forecasting 24 (6), 1592–1609. https://doi.org/10.1175/2009WAF2222230.1.
Knupp, K.R., Murphy, T.A., Coleman, T.A., Wade, R.A., Mullins, S.A., Schultz, C.J., Schultz, E.V., Carey, L., Sherrer, A., McCaul, E.W., Carcione, B., Latimer, S., Kula, A., Laws, K., Marsh, P.T., Klockow, K., 2014. Meteorological overview of the devastating 27 April 2011 tornado outbreak. Bull. Am. Meteorol. Soc. 95, 1041–1062. https://doi.org/10.1175/BAMS-D-11-00229.1.
Koshak, W.J., Solakiewicz, R.J., Blakeslee, R.J., Goodman, S.J., Christian, H.J., Hall, J. M., Bailey, J.C., Krider, E.P., Bateman, M.G., Boccippio, D.J., Mach, D.M., McCaul, E. W., Stewart, M.F., Buechler, D.E., Petersen, W.A., Cecil, D.J., 2004. North Alabama Lightning Mapping Array (LMA): VHF source retrieval algorithm and error analyses. J. Atmos. Oceanic Tech. 21, 543–558. https://doi.org/10.1175/1520-0426(2004)021%3C0543:NALMAL%3E2.0.CO;2.
Krehbiel, P.R., Thomas, R.J., Rison, W., Hamlin, T., Harlin, J., Davis, M., 2000. GPS-based mapping system reveals lightning inside storms. Eos, Transactions American Geophysical Union 81, 21–25. https://doi.org/10.1029/00EO00014.
Kumjian, M.R., Ryzhkov, A.V., 2008. Polarimetric Signatures in Supercell Thunderstorms. J. Appl. Meteorol. Climatol. 47, 1940–1961. https://doi.org/10.1175/2007JAMC1874.1.
Lebo, Z.J., Morrison, H., 2014. Dynamical effects of aerosol perturbations on simulated idealized squall lines. Mon. Weather Rev. 142 (3), 991–1009. https://doi.org/10.1175/MWR-D-13-00156.1.
Lin, Y., Kumjian, M.R., 2022. Influences of CAPE on hail production in simulated supercell storms. J. Atmos. Sci. 79 (1), 179–204. https://doi.org/10.1175/JAS-D-21-0054.1.
List, R., 1961. Physical methods and instruments for characterizing hailstones. Bull. Am. Meteorol. Soc. 42, 452–466. https://doi.org/10.1175/1520-0477-42.7.452.
List, R., 2014. New hailstone physics. Part I: heat and mass transfer (HMT) and growth. J. Atmos. Sci. 71, 1508–1520. https://doi.org/10.1175/JAS-D-12-0164.1.
Lu, J., Qie, X., Jiang, R., Xiao, X., Liu, D., Li, J., 2021. Lightning activity during convective cell mergers in a squall line and corresponding dynamical and thermodynamical characteristics. Atmos. Res. 256, 105555. https://doi.org/10.1016/j.atmosres.2021.105555.
Lu, J., Qie, X., Xiao, X., Jiang, R., Mansell, E.R., Fierro, A.O., 2022. Effects of convective mergers on the evolution of microphysical and electrical activity in a severe squall line simulated by WRF coupled with explicit electrification scheme. J. Geophys. Res. Atmos. 127 (16), e2021JD036398. https://doi.org/10.1029/2021jd036398.
Luque, M.Y., Bürgesser, R.E., Ruiz, J.J., 2023. Study of the correlation between electrical activity and the microphysics and dynamics of a real severe event using the WRF-ELEC model. Q. J. Roy. Meteorol. Soc. 149 (753), 1520–1539. https://doi.org/10.1002/QJ.4471.
MacGorman, D.R., Rust, W.D., Krehbiel, P., Rison, W., Bruning, E., Wiens, K., 2005. The electrical structure of two supercell storms during STEPS. Mon. Weather Rev. 133, 2583–2607. https://doi.org/10.1175/MWR2994.1.
Miyamoto, Y., 2021. Effects of number concentration of cloud condensation nuclei on moist convection formation. J. Atmos. Sci. 78, 3401–3413. https://doi.org/10.1175/JAS-D-21-0058.1.
Nakanishi, M., Niino, H., 2004. An improved Mellor-Yamada Level-3 model with condensation physics: its design and verification. Bound.-Lay. Meteorol. 112 (1), 1–31. https://doi.org/10.1023/B:BOUN.0000020164.04146.98.
Nakanishi, M., Niino, H., 2009. Development of an improved turbulence closure model for the atmospheric boundary layer. Journal of the Meteorological Society of Japan. Ser. II 87 (5), 895–912. https://doi.org/10.2151/JMSJ.87.895.
Nelson, S.P., 1987. The hybrid multicellular–supercellular storm — an efficient hail producer. Part II: general characteristics and implications for hail growth. J. Atmos. Sci. 44, 2060–2073. https://doi.org/10.1175/1520-0469(1987)044%3C2060:THMSEH%3E2.0.CO;2.
Ni, X., Huang, F., Hui, W., Xiao, H., 2023. Lightning evolution in hailstorms from the geostationary lightning mapper over the contiguous United States. J. Geophys. Res. Atmos. 128, e2023JD038578. https://doi.org/10.1029/2023JD038578.
Nishizawa, S., Yashiro, H., Sato, Y., Miyamoto, Y., Tomita, H., 2015. Influence of grid aspect ratio on planetary boundary layer turbulence in large-eddy simulations. Geosci. Model Dev. 8 (10), 3393–3419. https://doi.org/10.5194/gmd-8-3393-2015.
Nixon, C.J., Allen, J.T., Taszarek, M., 2023. Hodographs and skew Ts of hail-producing storms. Weather Forecast. 38 (11), 2217–2236. https://doi.org/10.1175/WAF-D-23-0031.1.
Park, H.S., Ryzhkov, A.V., Zrnić, D.S., Kim, K.E., 2009. The hydrometeor classification algorithm for the polarimetric WSR-88D: description and application to an MCS. Weather and Forecasting 24 (3), 730–748. https://doi.org/10.1175/2008WAF2222205.1.
Pruppacher, H.R., Klett, J.D., 1997. Microphysics of Clouds and Precipitation, 2nd ed. Kluwer Academic. 954 pp.
Rigo, T., Farnell, C., 2022. Characterisation of thunderstorms with multiple lightning jumps. Atmosphere 13 (2), 171. https://doi.org/10.3390/ATMOS13020171.
Rotunno, Richard, Klemp, Joseph B., Weisman, Morris L., 1988. A theory for strong, long-lived squall lines. J. Atmos. Sci. 45, 463–485. https://doi.org/10.1175/1520-0469(1988)045<0463:ATFSLL>2.0.CO;2.
Salinas, V., Bruning, E.C., Mansell, E.R., 2022. Examining the kinematic structures within which lightning flashes are initiated using a cloud-resolving model. J. Atmos. Sci. 79 (2), 513–530. https://doi.org/10.1175/JAS-D-21-0132.1.
Sato, Y., Nishizawa, S., Yashiro, H., Miyamoto, Y., Kajikawa, Y., Tomita, H., 2015. Impacts of cloud microphysics on trade wind cumulus: which cloud microphysics processes contribute to the diversity in a large eddy simulation? Progress in Earth and Planetary Science 2 (1). https://doi.org/10.1186/s40645-015-0053-6.
Sato, Y., Miyamoto, Y., Tomita, H., 2019. Large dependency of charge distribution in a tropical cyclone inner core upon aerosol number concentration. Prog Earth Planet Sci 6 (1), 1–13. https://doi.org/10.1186/S40645-019-0309-7/FIGURES/9.
Sato, Y., Hayashi, S., Hashimoto, A., 2022. Difference in the lightning frequency between the July 2018 heavy rainfall event over central Japan and the 2017 northern Kyushu heavy rainfall event in Japan. Atmos. Sci. Lett. 23, e1067. https://doi.org/10.1002/ASL.1067.
Saunders, C.P.R., Keith, W.D., Mitzeva, R.P., 1991. The effect of liquid water on thunderstorm charging. J. Geophys. Res. Atmos. 96, 11007–11017. https://doi.org/10.1029/91JD00970.
Schultz, C.J., Petersen, W.A., Carey, L.D., 2009. Preliminary development and evaluation of lightning jump algorithms for the real-time detection of severe weather. Journal of

Applied Meteorology and Climatology 48 (12), 2543–2563. https://doi.org/10.1175/2009JAMC2237.1.
Schultz, C.J., Petersen, W.A., Carey, L.D., 2011. Lightning and severe weather: a comparison between total and cloud-to-ground lightning trends. Weather and Forecasting 26 (5), 744–755. https://doi.org/10.1175/WAF-D-10-05026.1.
Schultz, C.J., Carey, L.D., Schultz, E.V., Blakeslee, R.J., 2015. Insight into the kinematic and microphysical processes that control lightning jumps. Weather and Forecasting 30 (6), 1591–1621. https://doi.org/10.1175/WAF-D-14-00147.1.
Schultz, C.J., Carey, L.D., Schultz, E.V., Blakeslee, R.J., 2017. Kinematic and microphysical significance of lightning jumps versus nonjump increases in total flash rate. Weather and Forecasting 32 (1), 275–288. https://doi.org/10.1175/WAF-D-15-0175.1.
Scotti, A., Meneveau, C., Lilly, D.K., 1993. GeneralizedSsmagorinsky model for anisotropic grids. Phys. Fluids A 5, 2306–2308.
Seiki, T., Nakajima, T., 2014. Aerosol effects of the condensation process on a convective cloud simulation. J. Atmos. Sci. 71, 833–853. https://doi.org/10.1175/JAS-D-12-0195.1.
Smagorinsky, J., 1963. General circulation experiments with the primitive equations I. The basic experiment. Monthly Weather Review 91 (3), 99–164. https://doi.org/10.1175/1520-0493(1963)091<0099:GCEWTP>2.3.CO;2.
Takahashi, T., 1978. Riming electrification as a charge generation mechanism in thunderstorms. J. Atmos. Sci. 35 (8), 1536–1548. https://doi.org/10.1175/1520-0469(1978)035<1536:reaacg>2.0.co;2.
Takayama, H., Niino, H., Watanabe, S., Sugaya, J., Studies, M. of T. A. P, 1997. Downbursts in the northwestern part of Saitama Prefecture on 8 September 1994. Journal of the Meteorological Society of Japan. Ser. II 75 (4), 885–905. https://doi.org/10.2151/JMSJ1965.75.4_885.
Takemi, T., 2006. Impacts of moisture profile on the evolution and organization of midlatitude squall lines under various shear conditions. Atmos. Res. 82 (1–2), 37–54. https://doi.org/10.1016/J.ATMOSRES.2005.01.007.
Ushio, T., Heckman, S.J., Christian, H.J., Kawasaki, Z.-I., 2003. Vertical development of lightning activity observed by the LDAR system: lightning bubbles. Journal of Applied Meteorology and Climatology 42 (2), 165–174. https://doi.org/10.1175/1520-0450(2003)042.
Wakimoto, R.M., 1985. Forecasting dry microburst activity over the high plains. Mon. Wea. Rev. 113, 1131–1143. https://doi.org/10.1175/1520-0493(1985)113<1131:FDMAOT>2.0.CO;2.
Weisman, M.L., Rotunno, R., 2004. "A theory for strong long-lived squall lines" revisited. J. Atmos. Sci. 61 (4), 361–382. https://doi.org/10.1175/1520-0469(2004)061.
Williams, E., Boldi, B., Matlin, A., Weber, M., Hodanish, S., Sharp, D., 1999. The behavior of total lightning activity in severe Florida thunderstorms. Atmos. Res. 51 (3–4), 245–265. https://doi.org/10.1016/S0169-8095(99)00011-3.
Wilson, J.W., Wakimoto, R.M., 2001. The discovery of the downburst: T. T. Fujita's contribution. Bull. Amer. Meteor. Soc. 82, 49–62. https://doi.org/10.1175/1520-0477(2001)082<0049:TDOTDT>2.3.CO;2.
Wilson, J.W., Roberts, R.D., Kessinger, C., McCarthy, J., 1984. Microburst wind structure and evaluation of doppler radar for airport wind shear detection. Journal of Climate and Applied Meteorology. American Meteorological Society. https://doi.org/10.1175/1520-0450(1984)023<0898:MWSAEO>2.0.CO;2.